

Rydberg excitons and polaritons in monolayer transition metal dichalcogenides in a magnetic field

David de la Fuente Pico,^{1,2} Jesper Levinsen,^{3,4} Emma Laird,⁵ Meera M. Parish,^{3,4} and Francesca Maria Marchetti^{1,2}

¹*Departamento de Física Teórica de la Materia Condensada,
Universidad Autónoma de Madrid, Madrid 28049, Spain*

²*Condensed Matter Physics Center (IFIMAC), Universidad Autónoma de Madrid, 28049 Madrid, Spain*

³*School of Physics and Astronomy, Monash University, Victoria 3800, Australia*

⁴*ARC Centre of Excellence in Future Low-Energy Electronics Technologies, Monash University, Victoria 3800, Australia*

⁵*ARC Centre of Excellence in Future Low-Energy Electronics and Technologies,
University of Queensland, Queensland 4072, Australia*

(Dated: October 2, 2024)

We develop a microscopic theory for excitons and exciton polaritons in transition metal dichalcogenide (TMD) monolayers under a perpendicular static magnetic field. We obtain numerically exact solutions for the ground and excited states, accounting for the interplay between arbitrarily large magnetic fields and light-matter coupling strengths. This includes the very strong coupling regime, where light-induced modifications of the exciton wavefunction become essential and the approximate coupled oscillator description breaks down. Our results show excellent agreement with recent experimental measurements of the diamagnetic shift of the ground and excited exciton states in WS₂, MoS₂, MoSe₂, and MoTe₂ monolayers. For polaritons, we consider experimentally relevant system parameters and demonstrate that the diamagnetic shifts of both the ground and excited states at high magnetic fields exhibit clear signatures of the very strong coupling regime, highlighting the necessity of our microscopic and numerically exact treatment over perturbative approaches. Furthermore, our microscopic approach allows us to evaluate the exciton-exciton and polariton-polariton interaction strengths. Comparing results specific to TMD monolayers with those applicable to quantum wells, we find that variational approaches overestimate the TMD excitons' interaction strength. We also observe that magnetic fields weaken the interaction strength for both excitons and polaritons, with a less pronounced effect in TMDs than in quantum wells, and that light-induced modifications to the matter component in TMD polaritons can enhance interaction strengths beyond those of purely excitonic interactions.

I. INTRODUCTION

Magneto-optical spectroscopy plays an essential role in investigating two-dimensional (2D) semiconductors [1] and is highly effective for manipulating and exploring the properties of excitons. The application of this technique to traditional 2D semiconductors, such as III-V [2, 3] and II-VI [4, 5] quantum wells (QWs), has a long history, where it has been instrumental in manipulating and analyzing exciton properties. In this context, a magnetic field in a perpendicular geometry has been used to distinguish and identify both the ground and excited exciton states. In addition, the resulting diamagnetic shifts provide valuable information about the exciton reduced mass, size, and spin, enabling a direct comparison of experimental results with Wannier-based exciton models [6–8].

The magnetic field acts as an in-plane confining potential, further binding the excitons and enhancing their coupling to light. This effect has been employed to strongly couple the ground and excited exciton states to light to form exciton polaritons (polaritons for short) when the QW is embedded into a microcavity [9–12]. Indeed, for III-V heterostructures, the Rabi couplings between the excited exciton states and a microcavity photon are hardly detectable at zero magnetic field, but are enhanced when a magnetic field is applied [13–15] and

can therefore be measured. Importantly, the diamagnetic shift of polariton modes has been proposed [16] and utilized [12, 17] as a method to confirm the realization of the very strong light-matter coupling regime. In this regime, the Rabi coupling approaches the exciton binding energy, resulting in the hybridization of different excitonic states within a single polariton state.

More recently, significant advances have been made in the study of atomically thin 2D semiconductors. In particular, transition metal dichalcogenide (TMD) monolayers are emerging as unique 2D optically active materials with remarkable properties arising from their low dimensionality and unique band structure, opening new directions of study in optoelectronics, as well as complementing those for traditional quantum well structures [18]. TMD monolayers have a direct bandgap together with valley- and spin-dependent selection rules, leading to potential applications in valleytronics, optoelectronics and the fabrication of nanophotonic devices [19–21]. Furthermore, they exhibit pronounced exciton resonances even at room temperature. Indeed, due to heavy carrier masses and reduced dielectric screening, excitons in TMD monolayers are characterized by very large binding energies, on the order of hundreds of meV [22–24]. Their strong coupling to light led to the first observation of room-temperature polaritons with TMD monolayers embedded in a microcavity [25, 26], and to the first observation of polariton states with excited exci-

ton states [27]. Similar to QWs, stacking multiple TMD monolayers inside an optical microcavity leads to an increase in the Rabi coupling towards the very strong coupling regime [28].

Magneto-optical measurements have already been employed for the quantitative analysis of TMD monolayer parameters and for gaining detailed insights into spin-valley physics — for a review, see Ref. [29]. As with III-V and II-VI quantum wells, exciton properties in TMD monolayers — such as their reduced mass, size, binding energy, and dependence on the dielectric environment — have been studied using magnetic fields [30–39]. The main differences for TMD monolayers in comparison to III-V and II-VI quantum wells are the much larger exciton binding energies and smaller radii, which require much stronger magnetic fields — on the order of tens of Tesla — to observe a significant diamagnetic shift in the exciton ground state. However, the higher exciton oscillator strengths facilitate the detection of excited states. In TMD monolayers such as MoS₂, MoSe₂, MoTe₂, and WS₂, high magnetic fields of up to 60 T [39] have made it possible to observe the first five Rydberg exciton states. The distinct shifts of the excited states provide a direct means to quantitatively compare experimental data with theoretical models.

In this paper, we develop a microscopic theory for excitons in a TMD monolayer under a perpendicular static magnetic field, as well as for polaritons when one or several monolayers are embedded in a microcavity. Numerically exact solutions are obtained for the ground and excited states for arbitrary large magnetic fields and light-matter coupling strengths, extending to the very strong coupling regime, where it is crucial to take light-induced modifications of the exciton wavefunction into account. Generalizing previous results valid for quantum wells [17], the numerically exact solution takes advantage of a mapping between the 2D hydrogen atom and the 2D harmonic oscillator. We find excellent agreement between our results and experimental measurements of the diamagnetic shift of the ground and excited exciton states for MoS₂, MoSe₂, MoTe₂, and WS₂ monolayers at high fields up to 60 T [39]. For polaritons we consider system parameters accessible to current experiments [28]. We demonstrate that the diamagnetic shift of the ground and excited states at large values of the magnetic field carry signatures of the very strong coupling regime between light and matter, that strongly differentiate our exact results from perturbative ones.

We furthermore employ a Born approximation to estimate the ground-state exciton-exciton and polariton-polariton interaction strengths and their dependence on the magnetic field. We evaluate these for TMD monolayers and for typical III-V quantum wells, thus allowing us to directly compare these two platforms. We find that the magnetic field decreases the interaction strength both between excitons and between polaritons, with a more pronounced effect for QWs compared to TMD monolayers, since the latter have substantially larger exciton

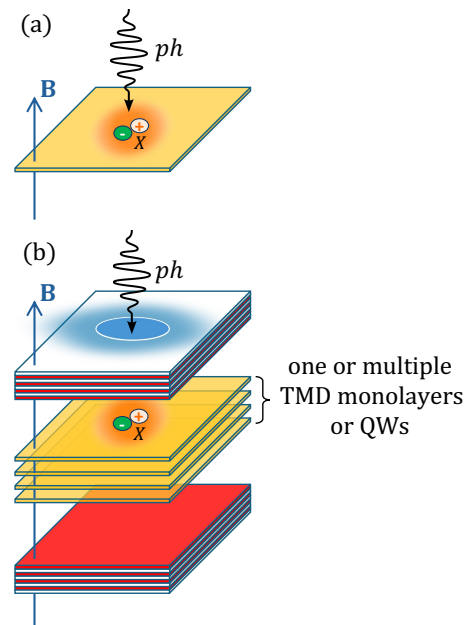


FIG. 1. Schematic representation of the two set-ups considered in this work. (a) A TMD monolayer or single quantum well in a perpendicular homogeneous magnetic field \mathbf{B} is optically excited by a resonant circularly polarized photon (ph) generating an electron-hole pair which form an exciton (X). (b) One or several encapsulated TMD monolayers or QWs in a magnetic field are embedded into an optical microcavity excited at normal incidence.

binding energies. For TMD excitons, we show that the use of hydrogenic variational wavefunctions [40] overestimates the interaction strength, leading to qualitatively incorrect results and highlighting the need for exact solutions. Finally, we demonstrate for TMD polaritons that incorporating light-induced modifications to the matter component can lead to interaction strengths that exceed those of purely excitonic interactions.

The paper is organized as follows: In Sec. II, we present the microscopic model describing TMD excitons and polaritons in a static magnetic field. The formalism required to obtain numerically exact solutions for the full Rydberg series of magnetoexcitons and magnetopolaritons is presented in Sec. III and Sec. IV, respectively. The results, along with comparisons to experimental data and predictions for future studies, are discussed in these respective sections. In Sec. V and Sec. VI, we evaluate the exciton-exciton and polariton-polariton interaction strengths, respectively, and discuss the effects of both a strong magnetic field and very strong coupling to light. Conclusions are drawn in Sec. VII.

II. MODEL

In this section, we introduce the microscopic model employed to describe conduction electron and valence

hole charges in a TMD monolayer that can form excitons. In addition, we include the possibility of describing cavity photons and their coupling to matter excitations when the monolayer is embedded in an optical microcavity (see Fig. 1). Our microscopic description allows us to capture non-perturbative effects arising from both a strong (perpendicular) magnetic field, as well as very strong light-matter interactions. Further, in this work we assume that electron-hole pairs are excited across the energy gap of a single valley by circularly polarized light, so that excitons are spin-valley polarized and we can for-

mally neglect these degrees of freedom.

The system Hamiltonian includes three terms: \hat{H}_m depicts the matter-only excitations, i.e., conduction electrons and valence holes, \hat{H}_C the cavity photon, and \hat{H}_{Cm} the interaction between light and matter:

$$\hat{H} = \hat{H}_m + \hat{H}_C + \hat{H}_{Cm}. \quad (1)$$

In the presence of a magnetic field, the electrons and holes in a TMD monolayer are described by the Hamiltonian (throughout this work we fix $\hbar = 1$)

$$\hat{H}_m = \sum_{\sigma=e,h} \int d\mathbf{r} \hat{\Psi}_{\sigma}^{\dagger}(\mathbf{r}) \frac{[-i\nabla + \frac{e}{c}\mathbf{A}(\mathbf{r})]^2}{2m_{\sigma}} \hat{\Psi}_{\sigma}(\mathbf{r}) + \frac{1}{2} \sum_{\sigma,\sigma'} \int d\mathbf{r}_1 d\mathbf{r}_2 \hat{\Psi}_{\sigma}^{\dagger}(\mathbf{r}_1) \hat{\Psi}_{\sigma'}^{\dagger}(\mathbf{r}_2) W_{\sigma\sigma'}(\mathbf{r}_1 - \mathbf{r}_2) \hat{\Psi}_{\sigma'}(\mathbf{r}_2) \hat{\Psi}_{\sigma}(\mathbf{r}_1), \quad (2)$$

where $\hat{\Psi}_{\sigma}^{\dagger}(\mathbf{r})$ ($\hat{\Psi}_{\sigma}(\mathbf{r})$) are the creation (annihilation) field operators for electrons and holes ($\sigma = e, h$) at the position \mathbf{r} , and $m_{e,h}$ their effective masses.¹ Note that, unless mentioned explicitly, throughout this work we measure the energies with respect to the bandgap energy E_g . The operators satisfy canonical anticommutation relations:

$$\{\hat{\Psi}_{\sigma}(\mathbf{r}), \hat{\Psi}_{\sigma'}^{\dagger}(\mathbf{r}')\} = \delta(\mathbf{r} - \mathbf{r}') \delta_{\sigma\sigma'} \quad (3a)$$

$$\{\hat{\Psi}_{\sigma}(\mathbf{r}), \hat{\Psi}_{\sigma'}(\mathbf{r}')\} = \{\hat{\Psi}_{\sigma}^{\dagger}(\mathbf{r}), \hat{\Psi}_{\sigma'}^{\dagger}(\mathbf{r}')\} = 0. \quad (3b)$$

In view of the fact that, later on, we are interested in evaluating polariton-polariton interaction properties, we find it convenient to work with a second quantization formalism in the real space representation. The model can equivalently be formulated within momentum space, see Ref. [17] for details.

We assume that the magnetic field $\mathbf{B} = \nabla \times \mathbf{A}(\mathbf{r}) = (0, 0, B)$ is uniform and oriented in the z direction, perpendicularly to the x - y plane of the TMD monolayer. We work in the symmetric gauge, where the vector potential is given by:

$$\mathbf{A}(\mathbf{r}) = \frac{1}{2} \mathbf{B} \times \mathbf{r} = \frac{B}{2} (-y, x, 0). \quad (4)$$

Note that this gauge choice is consistent with the Coulomb gauge $\nabla \cdot \mathbf{A}(\mathbf{r}) = 0$, employed when describing the coupling to light.

The last term in Eq. (2) depicts the attractive interaction between an electron and a hole $W_{eh}(\mathbf{r})$, leading to the formation of excitons, as well as the repulsion either between two electrons $W_{ee}(\mathbf{r})$ or two holes $W_{hh}(\mathbf{r})$ when

multiple electron-hole pairs are photo-excited:

$$W_{eh}(\mathbf{r}) = V(r) \quad (5a)$$

$$W_{ee}(\mathbf{r}) = W_{hh}(\mathbf{r}) = -V(r). \quad (5b)$$

For TMD monolayers, either encapsulated within two dielectrics or held in vacuum, the electron-hole interaction has been shown to be appropriately accounted for by the Rytova-Keldysh potential [41, 42] (throughout this work we use Gaussian units $4\pi\epsilon_0 = 1$, where ϵ_0 is the vacuum permittivity):

$$V(r) = -\frac{\pi e^2}{2r_0\epsilon} \left[H_0\left(\frac{r}{r_0}\right) - Y_0\left(\frac{r}{r_0}\right) \right]. \quad (6)$$

Here, $H_0(x)$ is the zeroth order Struve function and $Y_0(x)$ the zeroth-order Bessel function of the second kind. TMD monolayers are typically encapsulated, often with hexagonal boron nitride (hBN), which significantly enhances their optical quality [43, 44]. In Eq. (6), the influence of the surrounding materials, characterized by dielectric constants $\epsilon_{1,2}$, is modelled by introducing an effective dielectric constant $\epsilon = \frac{1}{2}(\epsilon_1 + \epsilon_2)$, while r_0 is the screening length. For a TMD monolayer having width d and dielectric constant ϵ_{ML} , the screening length is defined as $r_0 = d\epsilon_{ML}/(2\epsilon)$ [23]. In the strictly 2D limit ($d \rightarrow 0$) and in vacuum ($\epsilon = 1$), the screening length is defined in terms of the 2D polarizability of the monolayer χ_{2D} , as $r_0 = 2\pi\chi_{2D}$ [45]. The screening length r_0 marks the crossover between short- and long-range behavior: At short distances, the Rytova-Keldysh potential diverges as $\sim \ln r$, accounting for the confinement of field lines in the 2D plane. Instead, at large distances, it recovers the Coulomb potential dependence $\sim r^{-1}$. The non-local screening introduced by this potential has been shown to accurately describe exciton properties in TMD monolayers [23, 24, 45]. Furthermore, the Rytova-Keldysh potential is also commonly used to evaluate electron-electron and hole-hole interactions. However, its validity for more complex structures, such as trions, is a subject of debate [46].

¹ Strong experimental support for the applicability of the Wannier-Mott model and effective mass theory to describe the key properties of excitons in TMD monolayers first came from studies of exciton radii in WS_2 monolayers using magneto-optical reflectance spectroscopy [35].

The photonic part of the Hamiltonian is:

$$\hat{H}_C = \omega \hat{a}^\dagger \hat{a} , \quad (7)$$

where ω is the bare cavity energy (i.e., the cavity photon energy in absence of an embedded active medium [47]) and \hat{a}^\dagger (\hat{a}) is the creation (annihilation) operator for the cavity photon. For simplicity, we only consider a single cavity mode. This either corresponds to the case of a 0D cavity, such as fiber cavities [48], or to the case of a photon mode with zero in-plane momentum of a 2D microcavity excited at normal incidence — see Fig. 1(b). In this case, because of the photon mass being about 5 orders of magnitude smaller than the mass of matter excitations, we can account for the finite photon momentum by simply shifting the cavity photon frequency.

Finally, the Hamiltonian term describing the light-matter coupling is:

$$\hat{H}_{Cm} = \frac{g}{\sqrt{\mathcal{A}}} \left[\hat{a} \int d\mathbf{r} \hat{\Psi}_e^\dagger(\mathbf{r}) \hat{\Psi}_h^\dagger(\mathbf{r}) + \text{h.c.} \right] , \quad (8)$$

where g is the light-matter coupling strength and \mathcal{A} the system area. This term describes the creation (annihilation) of an electron-hole pair with zero electron-hole separation by absorption (emission) of a photon. Because of the effects of the active medium, approximating this interaction as effectively having zero range implies that the bare cavity energy ω needs to be renormalized by introducing the dressed photon energy [47], as discussed in detail in Sec. IV. Equation (8) allows us to describe very strong light-matter effects leading to the hybridization of different exciton states in the formation of polaritons. However, we assume that the TMD bandgap energy is much larger than the light-matter coupling strength, such that we can work in the rotating-wave approximation. This means that we do not describe the regime of ultrastrong coupling, where hybridization with different numbers of excitations occurs.

III. MAGNETOEXCITONS

In this section, we describe the formalism necessary to study the properties of excitons in TMD monolayers in a perpendicular magnetic field. A numerically exact microscopic theory of quantum well excitons in a perpendicular magnetic field has been already developed in Ref. [17] by making use of an exact mapping between the 2D harmonic oscillator and the 2D hydrogen atom. It was shown that this allowed a very efficient numerical solution of the problem, for any strength of the magnetic field. Here, we generalize those results valid for Coulomb interactions to the case of a Rytova-Keldysh potential, thus allowing us to describe current experiments on TMD monolayers. In particular, we demonstrate that our theory agrees very well with the exciton diamagnetic shift measured in recent magneto-optical experiments in Ref. [39]. We first review the formal steps followed to exactly solve the problem numerically, including the possibility of describing

states with any orbital angular momentum, and the necessary adaptation to the case of TMD monolayers.

In the presence of a homogeneous perpendicular magnetic field, the translational symmetry is preserved while the total linear momentum of an electron-hole pair is no longer conserved. Instead, the conserved quantity is the total magnetic momentum $\hat{\mathbf{K}}$ (the generator of translations), defined as

$$\hat{\mathbf{K}} = -i\nabla_{\mathbf{r}_e} - \frac{e}{c} \mathbf{A}(\mathbf{r}_e) - i\nabla_{\mathbf{r}_h} + \frac{e}{c} \mathbf{A}(\mathbf{r}_h) = -i\nabla_{\mathbf{R}} - \frac{e}{2c} \mathbf{B} \times \mathbf{r} , \quad (9)$$

where

$$\mathbf{R} = \frac{m_e \mathbf{r}_e + m_h \mathbf{r}_h}{m_e + m_h} \quad (10a)$$

$$\mathbf{r} = \mathbf{r}_e - \mathbf{r}_h , \quad (10b)$$

are the center of mass and relative positions, respectively. Because of this, the most general single exciton state in the center of mass frame can be written as

$$|X_{\mathbf{K}}\rangle = \hat{X}_{\mathbf{K}}^\dagger |0\rangle , \quad (11)$$

where the creation operator of an exciton with total magnetic momentum \mathbf{K} is

$$\hat{X}_{\mathbf{K}}^\dagger = \frac{1}{\sqrt{\mathcal{A}}} \int d\mathbf{r}_e d\mathbf{r}_h e^{i(\mathbf{K} + \frac{e}{2c} \mathbf{B} \times \mathbf{r}) \cdot \mathbf{R}} \times \varphi_{\mathbf{K}}(\mathbf{r}) \hat{\Psi}_e^\dagger(\mathbf{r}_e) \hat{\Psi}_h^\dagger(\mathbf{r}_h) , \quad (12)$$

where $\varphi_{\mathbf{K}}(\mathbf{r})$ is the wavefunction describing the relative motion of the electron and hole. Equation (12) is referred to as the Lamb transformation and it was introduced first by Lamb in Ref. [49] for the hydrogen atom and later adapted to the exciton problem by Gor'kov and Dzyaloshinskii in Ref. [50].

In order to derive the Schrödinger equation satisfied by the exciton wavefunction, we first evaluate the expectation value of the matter Hamiltonian (2) for the state (11):

$$\langle X_{\mathbf{K}} | \hat{H}_m | X_{\mathbf{K}} \rangle = \int d\mathbf{r} \varphi_{\mathbf{K}}^*(\mathbf{r}) \hat{H}'_m \varphi_{\mathbf{K}}(\mathbf{r}) , \quad (13)$$

with

$$\hat{H}'_m = \left[-\frac{\nabla_{\mathbf{r}}^2}{2\mu} - i \frac{e\eta}{2\mu c} \mathbf{B} \cdot (\mathbf{r} \times \nabla_{\mathbf{r}}) + \frac{e^2}{8\mu c^2} (\mathbf{B} \times \mathbf{r})^2 + \frac{e}{Mc} (\mathbf{K} \times \mathbf{B}) \cdot \mathbf{r} + \frac{\mathbf{K}^2}{2M} + V(r) \right] , \quad (14)$$

where $\mu = \frac{m_e m_h}{m_e + m_h}$ and $M = m_e + m_h$ are the exciton reduced and total masses, respectively, while $\eta = (m_h - m_e)/(m_e + m_h)$. The first and second terms of this expression can be rewritten in terms of the z -component of the relative orbital angular momentum operator $\hat{L}_z = -ix\partial_y + iy\partial_x = -i\partial_\theta$ (with eigenvalue l_z):

$$-i \frac{e\eta}{2\mu c} \mathbf{B} \cdot (\mathbf{r} \times \nabla_{\mathbf{r}}) = \frac{\omega_{c,e} - \omega_{c,h}}{2} \hat{L}_z \quad (15a)$$

$$-\nabla_{\mathbf{r}}^2 = -\partial_r^2 - \frac{1}{r} \partial_r + \frac{\hat{L}_z^2}{r^2}, \quad (15b)$$

where $\omega_{c,j} = \frac{eB}{m_j c}$ ($j = e, h$) are the electron and hole cyclotron frequencies. Equation (15a) corresponds to a simple Zeeman shift which only affects the exciton's energy and not the exciton wavefunction, since orbital angular momentum l_z is a good quantum number. In addition, we focus on s -wave exciton states where $l_z = 0$ in (15), since one-photon transitions in TMD monolayers only allow the excitations of isotropic exciton states, i.e., those with s -wave symmetry and zero relative orbital angular momentum. Finite orbital angular momentum excitonic states are also referred to as 'dark' and cannot be accessed with linear optics. However, two-photon transitions can allow one to access dark excitons with odd parity [51]. Dark excitons can alternatively be detected by the application of a weak static in-plane electric field, which can induce orbital hybridization between Rydberg excitonic states with different angular momenta [52]. We investigate the extent to which our theoretical approach can be utilized to study excitons with finite orbital angular momentum in Appendix D.

A normally incident photon generates an electron-hole pair with zero center of mass momentum and zero separation, i.e., with magnetic momentum $\mathbf{K} = 0$. Since the magnetic momentum is a good quantum number, we can set it to zero from now on. In this case, the Schrödinger equation for the relative exciton wavefunction $\varphi_{\mathbf{0}}(\mathbf{r}) \equiv \varphi(r)$ reads as:

$$E\varphi(r) = \left[-\frac{1}{2\mu} \left(\frac{d^2}{dr^2} + \frac{1}{r} \frac{d}{dr} \right) + \frac{\mu\omega_c^2}{2} r^2 + V(r) \right] \varphi(r), \quad (16)$$

where $\omega_c = \frac{eB}{2\mu c}$ is the exciton cyclotron frequency.

The Schrödinger equation (16) can be solved perturbatively in the two regimes of weak and strong magnetic field. In the weak magnetic field limit, i.e., when $\omega_c \ll |E_{ns}^{B=0}|$, where $|E_{ns}^{B=0}|$ is the ns exciton binding energy for zero magnetic field, the perturbative expression for the exciton energy reads as:

$$E_{ns} \simeq E_{ns}^{B=0} + \frac{\mu\omega_c^2}{2} \langle r^2 \rangle_{ns}, \quad (17)$$

where $\langle r^2 \rangle_{ns}$ is the squared mean radius of the exciton, evaluated in the zero magnetic field limit. The electron-hole relative wavefunctions can also be evaluated perturbatively in this limit as:

$$\varphi_{ns}(r) \simeq \varphi_{ns}^{B=0}(r) + \frac{\mu\omega_c^2}{2} \sum_{m \neq n} \frac{\langle m|r^2|n \rangle}{E_{ns}^{B=0} - E_{ms}^{B=0}} \varphi_{ms}^{B=0}(r), \quad (18)$$

where $\langle m|r^2|n \rangle = \int d\mathbf{r} \varphi_{ms}^{B=0*}(r) r^2 \varphi_{ns}^{B=0}(r)$. In the opposite limit of a strong magnetic field, when $\omega_c \gg |E_{ns}^{B=0}|$, one instead has [6]

$$E_{ns} \simeq \omega_c \left[(2n-1) + \mathcal{O} \left(\frac{1}{\sqrt{\omega_c}} \right) \right]. \quad (19)$$

In the regime of intermediate magnetic field strengths, Eq. (16) has to be solved numerically. This can be carried out efficiently by mapping the 2D harmonic oscillator problem into the 2D hydrogen problem, as already discussed in Refs. [17, 53]. We thus perform the change of variables $\rho = \frac{r^2}{8a_X^2}$ and $\bar{E} = E/R_X$, where R_X and a_X are the exciton Rydberg and Bohr radius,

$$R_X = \frac{2\mu e^4}{\varepsilon^2} = \frac{1}{2\mu a_X^2} \quad a_X = \frac{\varepsilon}{2\mu e^2}. \quad (20)$$

These are the energy and length scales characterizing the 2D hydrogenic exciton problem for pure Coulomb interaction [54], i.e., $R_X = \lim_{r_0 \rightarrow 0} |E_{1s}^{B=0}|$. The change of variables results in the following dimensionless equation:

$$\frac{2\bar{E}}{\rho} \bar{\varphi}(\rho) = \left[-\frac{d^2}{d\rho^2} - \frac{1}{\rho} \frac{d}{d\rho} + 4\bar{\omega}_c^2 + \tilde{V}(\rho) \right] \bar{\varphi}(\rho), \quad (21)$$

where $\bar{\varphi}(\rho) = a_X \varphi(\mathbf{r})$, $\bar{\omega}_c = \omega_c/R_X$, and $\tilde{V}(\rho) = \frac{2V(\sqrt{8a_X^2\rho})}{R_X\rho}$. We can now carry out the Fourier transform from the rescaled real coordinate ρ to the rescaled reciprocal space $\boldsymbol{\kappa}$, by applying $\int d\rho e^{-i\boldsymbol{\kappa}\cdot\rho} \{ \cdot \}$ to both sides of Eq. (21), obtaining:

$$\bar{E} \sum_{\boldsymbol{\kappa}'} \frac{4\pi \bar{\varphi}_{\boldsymbol{\kappa}'}}{|\boldsymbol{\kappa} - \boldsymbol{\kappa}'|} = (\boldsymbol{\kappa}^2 + 4\bar{\omega}_c^2) \bar{\varphi}_{\boldsymbol{\kappa}} + \sum_{\boldsymbol{\kappa}'} \tilde{V}_{|\boldsymbol{\kappa}-\boldsymbol{\kappa}'|} \bar{\varphi}_{\boldsymbol{\kappa}'}, \quad (22)$$

where $\boldsymbol{\kappa} = (\kappa, \phi)$, we use the notation $\sum_{\boldsymbol{\kappa}} \equiv \int \frac{d\boldsymbol{\kappa}}{(2\pi)^2} = \int_0^\infty \frac{d\kappa \kappa}{2\pi} \int_0^{2\pi} \frac{d\phi}{2\pi}$, and $\tilde{V}_{\boldsymbol{\kappa}} = \int d\rho e^{-i\boldsymbol{\kappa}\cdot\rho} \tilde{V}(\rho)$. The analytic expression for $\tilde{V}_{\boldsymbol{\kappa}}$ is given in Eq. (B1). Note that the previously obtained eigenfunctions must be properly normalized in order to ensure that

$$1 = \int d\mathbf{r} |\varphi(r)|^2 = \int d\rho \frac{4}{\rho} |\bar{\varphi}(\rho)|^2 = 8\pi \sum_{\boldsymbol{\kappa}, \boldsymbol{\kappa}'} \frac{\bar{\varphi}_{\boldsymbol{\kappa}} \bar{\varphi}_{\boldsymbol{\kappa}'}^*}{|\boldsymbol{\kappa} - \boldsymbol{\kappa}'|}. \quad (23)$$

This can easily be achieved if we take $\bar{\varphi}_{\boldsymbol{\kappa}} \rightarrow \bar{\varphi}_{\boldsymbol{\kappa}}/\mathcal{N}$ with $\mathcal{N}^2 = 8\pi \sum_{\boldsymbol{\kappa}, \boldsymbol{\kappa}'} \frac{\bar{\varphi}_{\boldsymbol{\kappa}} \bar{\varphi}_{\boldsymbol{\kappa}'}^*}{|\boldsymbol{\kappa} - \boldsymbol{\kappa}'|}$. This change is implicitly assumed throughout the remainder of this section.

The Schrödinger equation in rescaled momentum $\boldsymbol{\kappa}$ space (22) can be readily solved by direct diagonalization once the rescaled momentum $\boldsymbol{\kappa}$ is discretized on a grid. In particular, we choose to use a Gauss-Legendre quadrature [55]. Both the Rytova-Keldysh term $\tilde{V}_{|\boldsymbol{\kappa}-\boldsymbol{\kappa}'|}$, as well as the 2D Coulomb-like term $\frac{4\pi}{|\boldsymbol{\kappa}-\boldsymbol{\kappa}'|}$ have a pole for $\boldsymbol{\kappa} = \boldsymbol{\kappa}'$. In order to deal with these singularities, we

	hBN-WS ₂	GaAs QW
Effective dielectric constant ε	4.35	12.9
Screening length r_0 (nm)	0.78	0
Reduced mass μ (m_0)	0.175	0.041
1s binding energy ϵ_b (meV)	178.8	13.5

TABLE I. Model parameters used in the main text to describe hBN-encapsulated WS₂ experiments of Ref. [39] and typical GaAs quantum well experiments — see, e.g., Ref. [12]. Here, m_0 is the bare electron mass. In the last row we specify the obtained values of the 1s exciton binding energies for the two systems — note that, for QWs, the binding energy ϵ_b coincides with the exciton Rydberg R_X (20). Note also that we use a different definition of r_0 than Ref. [39] ($r_0^{[39]} = r_0\varepsilon$).

implement the subtraction scheme proposed in Ref [17]. This subtraction scheme allows us to cancel the singularities at $\kappa = \kappa'$ in both terms,² without fictitiously removing them, thus significantly accelerating the numerical convergence. Details are given in appendix B. Note that, in Eq. (22), $\bar{\omega}_c$ plays the role of an eigenvalue, while \bar{E} corresponds to the strength of a pure Coulomb interaction. Equivalently, the matrix in (κ, κ') space multiplying the \bar{E} term can be inverted to treat instead \bar{E} as an eigenvalue.

By applying the numerical scheme just described to solve the Schrödinger equation for the s -states, we obtain the numerically exact exciton energies and eigenfunctions for the Rydberg series of ns states in a TMD monolayer in the presence of a magnetic field of arbitrary value. We have checked that all our results are converged with respect to the number of points on the momentum grid. We compare our results with the experimental measurements of the exciton diamagnetic shift of Ref. [39] where the magnetic field dependence of the exciton Rydberg energies for hBN-encapsulated WS₂, MoTe₂, MoSe₂, and MoS₂ were obtained for a magnetic field up to 60 T. As we show, the agreement between our numerics and the experimental data is excellent. In the main text, we illustrate the specific case of an encapsulated WS₂ monolayer, while the results for the other TMD monolayers are reported in Appendix C.

The parameters used to describe the hBN-encapsulated WS₂ results presented in the main text are listed in Table I. These parameters have been extracted in Ref. [39] by making use of the perturbative expressions (17) and (19) of the exciton diamagnetic shift. In particular, the diamagnetic shifts of the most weakly bound states observed in experiments, the 4s and 5s states, provide, for a strong magnetic field, upper and lower bounds for the exciton reduced mass μ which are independent of the specific dielectric parameters. Once a range of μ is determined, r_0 and ε can be extracted from the diamagnetic shifts of the more tightly bound 1s

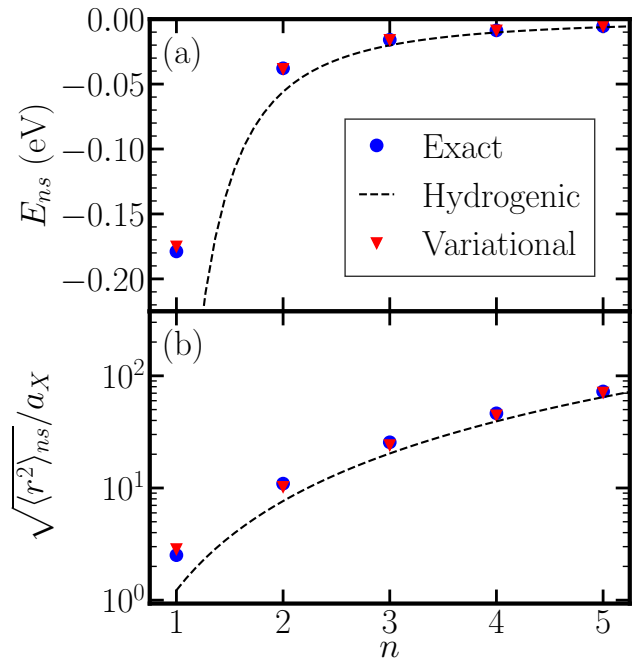


FIG. 2. (a) Rydberg exciton energies for ns states at zero magnetic field (blue dots) as a function of the principal quantum number n for system parameters describing the hBN-encapsulated WS₂ monolayer experiment of Ref. [39] (see Table I). The dashed black line is the hydrogenic energy (A2) for a pure Coulomb interaction and with the same choice of reduced mass μ and dielectric constant ε . The red triangles are obtained variationally with trial hydrogenic solutions where the exciton Bohr radius is employed as the variational parameter (see appendix A). (b) Exciton root-mean-square radius ($a_X = 0.66$ nm). The color code is the same for both panels.

and 2s states at small magnetic fields. A more precise estimation of the reduced mass can be obtained by numerical solution in intermediate regimes. We show that the choice of parameters listed in Table I for WS₂ leads to an exceptional agreement of our numerical results with the experimental measurements. Finally, in the same table we also consider, for comparison, the typical parameters describing GaAs quantum well experiments (see, e.g., Ref. [12]). In this case exciton properties are well described by a pure Coulomb interaction potential.

1. Zero magnetic field

First we explore the results in the limit of zero magnetic field and illustrate the deviations of the Rytova-Keldysh interaction potential from the hydrogenic solutions [24], as well as the limitations of a variational approach based on hydrogenic states [23, 35, 40]. We consider the parameters describing the hBN-encapsulated WS₂ experiments of Ref. [39] listed in Table I and obtain an exciton binding energy of $\epsilon_b = |E_{1s}^{B=0}| = 178.8$ meV for the 1s exciton, consistent with the measured value

² Note that the subtraction scheme should also be applied to evaluate the normalization constant, \mathcal{N}^2 , below Eq. (23).

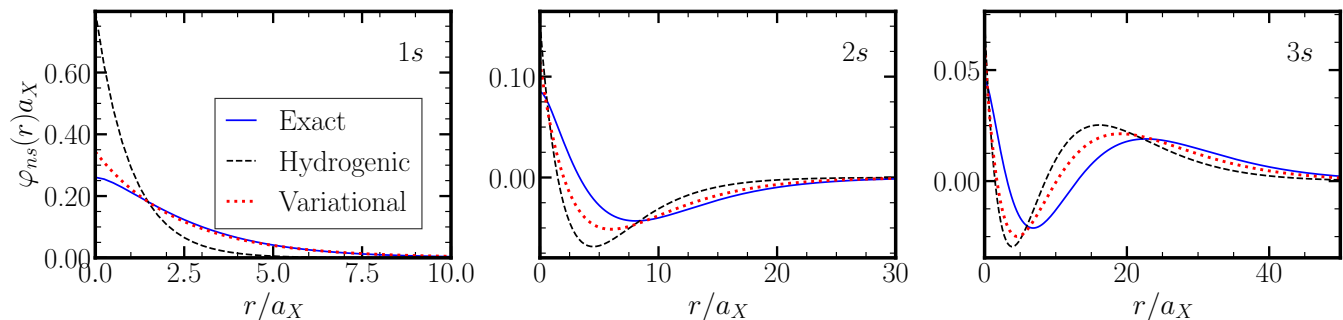


FIG. 3. Electron-hole wavefunctions $\varphi_{ns}(r)$ in real space at zero magnetic field for the first three states of the Rydberg ns series. Parameters have been fixed to describe hBN-encapsulated WS_2 monolayer (see Table I, $a_X = 0.66$ nm) and the color code is the same as in Fig. 2.

(180 ± 3) meV in Ref. [39]. In Fig. 2(a) we plot the energies of the first five s -wave exciton states E_{ns} . In order to show the deviations from the hydrogenic series obtained for a pure Coulomb interaction (i.e., by setting $r_0 = 0$), we compare our numerical results for E_{ns} with E_{ns}^{hyd} obtained for the same choice of effective dielectric constant ε and reduced mass μ — see Eq. (A2). As already discussed in the literature [24], the effect of the non-local screening is clearly visible for the lowest energy states, which are the most affected by screening. For higher excited states, screening effects are reduced as they are large compared to r_0 . For our particular choice of parameters, the $n > 3$ states are already hydrogen-like.

In addition, we compare the numerically exact results with those obtained from a variational approach with hydrogenic wavefunctions using a variational Bohr radius, as previously employed [23, 35, 40] (see Appendix A for details). The variational parameters obtained with this procedure are summarized in Table II. We observe that the variational results for the exciton energies E_{ns} match very well the numerically exact values, with a maximum deviation for the $1s$ state of about $\sim 2.2\%$. As n grows, the states become more hydrogenic and the matching between exact and variational results improves. The same applies to the exciton root-mean-square radius, plotted in Fig. 2(b). Minor deviations occur between the variational and the exact approach, which vanish for excited states, in agreement with previous work [23, 24, 35].

However, as illustrated in Fig. 3, the overall shape of the exciton wavefunction is modified by the Rytova-Keldysh potential in a way which cannot be captured by the variational wavefunction, with differences persisting even for excited states. We will argue in Sec. VI that these differences lead to qualitatively different results for the exciton-exciton interaction strength when compared with previous results in Ref. [40].

2. Finite magnetic field

We now consider the effects of a static magnetic field applied perpendicularly to the TMD monolayer. The field strengths are taken to be up to 60 T as in the experiments of Ref. [39]. We plot in Fig. 4 the exciton energies of the first five s -states as a function of the magnetic field, finding excellent agreement between theory and experiment. When comparing numerically exact results with the perturbative expansion (17) valid in the low-field limit, we observe that the $1s$ state is accurately described by the quadratic perturbative term. Indeed, the large binding energy of the $1s$ state is such that the condition $\epsilon_b = |E_{1s}^{B=0}| \gg \omega_c$ is satisfied for values of the magnetic field up to 60 T. However, for the $2s$ state, the perturbative expression becomes inadequate for magnetic field strengths larger than 45 T. For higher energy states, the binding energy $|E_{ns}^{B=0}|$ strongly decreases with n and the perturbative results lose validity for increasingly smaller values of the magnetic field.

Even though the exciton energy E_{ns} grows with the magnetic field, the continuum also shifts upwards such that the excitons effectively become more strongly bound with B , similarly to the case of pure Coulomb interactions [6, 8, 17]. Indeed, for a given n the continuum starts at the Landau energy $E_{Ns}^{Landau} = \frac{1}{2}(\omega_{c,e} + \omega_{c,h})(N+1) = \omega_c(N+1)$ [56], where the Landau level index N and the exciton principal quantum number n are related by $N = 2(n-1)$. To illustrate this, we plot in Fig. 5(a) the energy difference $\Delta E_{ns} = E_{ns} - (2n-1)\omega_c$, the absolute value of which coincides with the exciton binding energy. ΔE_{ns} becomes more negative as the magnetic field increases and excitons become more bound. Note that, for the magnetic field values considered, the $1s$ state energy E_{1s} is well described by the perturbative small field quadratic expression and thus, the dominant magnetic field dependence of $\Delta E_{1s} = E_{1s} - \omega_c$ at small values of B is linear.

The increase in the exciton binding energy with the magnetic field is accompanied by a reduction in the exciton size, as shown in Fig. 5(b). This can be evaluated

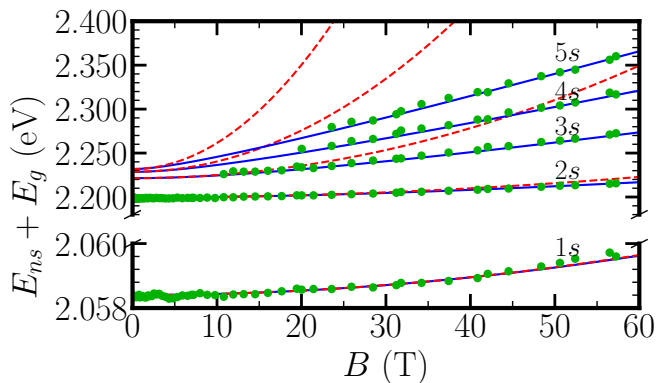


FIG. 4. Comparison of the exciton diamagnetic shift for the first five s -states obtained from the numerically exact solution of Eq. (22) (solid blue lines) with the experimental results for hBN-encapsulated WS₂ of Ref. [39] (green dots). Dashed red lines are results of perturbation theory for a weak magnetic field (17). The energy gap is set to the experimentally determined value $E_g = 2.23725$ eV.

in κ -space as [17]:

$$\frac{\langle r^2 \rangle}{a_X^2} = \frac{1}{a_X^2} \int d\mathbf{r} r^2 |\varphi(r)|^2 = 32 \sum_{\kappa} |\bar{\varphi}_{\kappa}|^2, \quad (24)$$

where we have used the normalization condition (23).

Finally, we study how the magnetic field affects the exciton oscillator strength, i.e., the exciton's ability to couple to light. This is proportional to the probability of recombination of the electron-hole pair, i.e., to $|\varphi(r=0)|^2$ [54]. The probability amplitude $\varphi(r=0)$ can be computed as:

$$\varphi(r=0) = \frac{1}{a_X} \bar{\varphi}(\rho=0) = \frac{1}{a_X} \sum_{\kappa} \bar{\varphi}_{\kappa}. \quad (25)$$

We show in Fig. 5(c) the evolution of $\varphi(0)$ with the magnetic field. The increase of the exciton binding energy with the magnetic field is accompanied by an increase of the exciton's ability to couple to light. Similarly to GaAs QWs, the effect of the magnetic field becomes more relevant for excited states which have a smaller binding energy. However, in TMD monolayers, the binding energy and oscillator strength decrease slower with n compared to the hydrogenic series. Because of this, the effect of an applied magnetic field in modifying the relative wavefunction is weaker than the results found in Ref. [17] for the case of GaAs quantum wells.

IV. MAGNETOPOLARITONS

We now turn to the effects of a strong perpendicular magnetic field on a TMD monolayer embedded in a microcavity. In this scenario, the excitons become coupled to the cavity photon mode. Denoting the strength of

the coupling to the $1s$ exciton by $\Omega/2$, if the Rabi coupling Ω exceeds both the exciton and photon linewidths, the reversible energy transfer between excitons and cavity photons leads to the formation of magnetopolaritons. When the coupling strength becomes a sizeable fraction of the exciton binding energy ϵ_b , also referred to as the very strong coupling regime, the light-matter interaction hybridizes different excitonic states, leading to modifications of the electron-hole pair wavefunction [47]. The use of magnetic field as a tool for investigating and manipulating polaritons has already been proposed for III-V heterostructures [9–11]. For the same structures, it has also been proposed as a method to verify the regime of very strong light-matter coupling [12, 17]. Indeed, in this configuration the magnetic field is employed to probe modifications of the electron-hole wavefunction due to the very strong coupling to light.

The very strong coupling regime can be easily accessed experimentally in III-V and II-VI heterostructures by embedding multiple quantum wells into the microcavity [57, 58], since the Rabi splitting Ω grows as the square root of the number of quantum wells. In particular, in Ref. [12], it was possible to reach $\Omega/\epsilon_b \simeq 1.3$ (with $\epsilon_b = R_X = 13.5$ meV) by embedding 28 quantum wells in stacks of four at the seven central antinodes of the cavity light field, thus increasing Ω from 3.8 meV for one quantum well, to $\Omega = 17.4$ meV for 28 quantum wells.

In TMD monolayers, the exciton binding energy is about one order of magnitude larger than in III-V quantum wells such as GaAs (see Table I), and likewise the exciton oscillator strength is also much larger than for QWs. Recently, an increase of the Rabi splitting has been achieved, from 36 meV for one WS₂ monolayer embedded into a planar microcavity to 72 meV for 4 embedded monolayers [28]. If $\epsilon_b = 178.8$ meV, this implies that $\Omega/\epsilon_b \simeq 0.4$. Increasing the number of embedded monolayers, one can reach larger values of Ω/ϵ_b . We will fix later the specific value $\Omega = 100$ meV ($\Omega/\epsilon_b \simeq 0.6$) and show that clear signatures of the very strong coupling regime and hybridization of different excitonic states are accessible in current experiments [28].

We briefly review the derivation of the Schrödinger equations for magnetopolaritons. These were first obtained in Ref. [17]. Here, however, we employ a second quantization formalism in real space (1) since this will allow us to generalize our results to the case of two magnetopolaritons and to evaluate their interaction strength. A polariton state with $\mathbf{K} = 0$,

$$|P_0\rangle = \hat{P}_0^\dagger |0\rangle, \quad (26)$$

can be written by considering a superposition between the exciton state (11) and a photon:

$$\hat{P}_0^\dagger = \frac{1}{\sqrt{\mathcal{A}}} \int d\mathbf{r}_e d\mathbf{r}_h e^{i\left[\frac{e}{2c}\mathbf{B}\times(\mathbf{r}_e-\mathbf{r}_h)\right]\cdot\frac{m_e\mathbf{r}_e+m_h\mathbf{r}_h}{m_e+m_h}} \times \varphi(|\mathbf{r}_e-\mathbf{r}_h\rangle) \hat{\Psi}_e^\dagger(\mathbf{r}_e) \hat{\Psi}_h^\dagger(\mathbf{r}_h) + \gamma \hat{a}^\dagger, \quad (27)$$

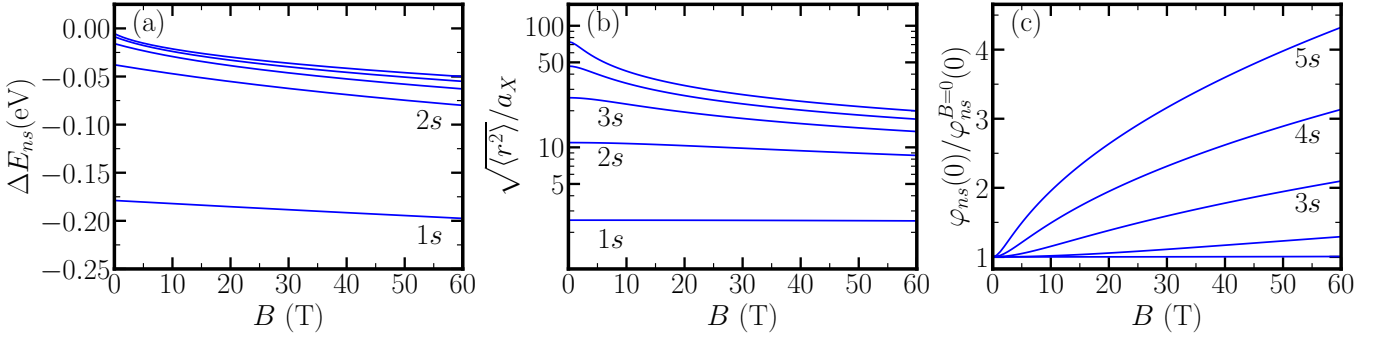


FIG. 5. (a) Exciton energy shift from the continuum (the Landau energy of a free electron and hole) $\Delta E_{ns} = E_{ns} - (2n - 1)\omega_c$. (b) Root-mean-square electron-hole separation. (c) Normalized exciton oscillator strength. System parameters are for a hBN-encapsulated WS₂ monolayer and are listed in Table I and $a_X = 0.66$ nm.

where $\varphi(r)$ is the wavefunction describing the electron and hole relative motion and γ is the photon amplitude. The normalization requires that

$$\langle P_0 | P_0 \rangle = 1 = \int d\mathbf{r} |\varphi(r)|^2 + |\gamma|^2. \quad (28)$$

The coupled equations for the exciton and photon amplitudes can be found by minimizing the functional $\langle P_0 | E - \hat{H} | P_0 \rangle$, obtaining:

$$\left[E + \frac{1}{2\mu} \left(\frac{d}{dr^2} + \frac{1}{r} \frac{d}{dr} \right) - \frac{\mu\omega_c^2}{2} r^2 - V(r) \right] \varphi(r) = g\gamma\delta(\mathbf{r}) \quad (29a)$$

$$(E - \omega)\gamma = g \int d\mathbf{r} \varphi(r) \delta(\mathbf{r}). \quad (29b)$$

As already discussed in Ref. [17], the presence of the Dirac delta $\delta(\mathbf{r})$ in Eq. (29a) implies that the relative wavefunction $\varphi(r)$ diverges as $\ln(r)$ when $r \rightarrow 0$. The divergent part of $\varphi(r)$ can be isolated by considering instead

$$\varphi(r) = \beta(r) - \frac{g\gamma\mu}{\pi} K_0 \left(\frac{r\sqrt{\epsilon_b}}{a_X} \right), \quad (30)$$

where $K_0(x)$ is the zeroth-order modified Bessel function of the second kind. Here, $K_0(r)$ diverges as $\ln(r)$ when r goes to zero, thus cancelling out the delta function $\delta(\mathbf{r})$ term in Eq. (29a). On the other hand, $\beta(r)$ is a regular function at $r = 0$.

The logarithmic divergence of $K_0(r)$ when $r \rightarrow 0$ leads to the formal divergence of the integral on the right-hand side of Eq. (29b), which requires us to renormalize the photon energy ω , as already discussed in Ref. [47]. Note that because the divergence occurs at zero distance, the magnetic field does not interfere with the renormalization process. Indeed, following [17], the formal divergence of Eq. (29b) can be dealt with by properly relating the physical observables of the system with the parameters of the microscopic model. Observables in experiments are the photon energy in the presence of an active medium,

or, equivalently, the photon energy detuning δ measured from the 1s exciton energy $E_{1s}^{B=0} = -\epsilon_b$, and the Rabi splitting Ω . Both quantities are measured in the absence of a magnetic field. In the limit $\Omega \ll \epsilon_b$, i.e., away from the very strong coupling regime, one expects to recover the polariton energies obtained from a two coupled oscillator model (2-COM)

$$E \begin{pmatrix} \beta \\ \gamma \end{pmatrix} = \begin{pmatrix} -\epsilon_b & \Omega/2 \\ \Omega/2 & \delta - \epsilon_b \end{pmatrix} \begin{pmatrix} \beta \\ \gamma \end{pmatrix}, \quad (31)$$

where $|\gamma|^2$ and $|\beta|^2 = 1 - |\gamma|^2$ are the photon and exciton photon fractions, respectively. Indeed, in this limit, and away from the resonance with excited exciton states, the exciton wavefunction is barely modified by light. The eigenvalues of the 2-COM are the usual lower (LP) and upper polariton (UP) modes with energies:

$$E_{LP,UP} = -\epsilon_b \pm \frac{1}{2}(\delta \mp \sqrt{\delta^2 + \Omega^2}), \quad (32)$$

and Hopfield coefficients:

$$\gamma_{LP,UP} = \mp \sqrt{\frac{1}{2} \left(1 \mp \frac{\delta^2}{\sqrt{\delta^2 + \Omega^2}} \right)}. \quad (33)$$

One can show [47] that Eqs. (29) at zero magnetic field and in the limit $\Omega \ll \epsilon_b$ recover those of the 2-COM for the following expressions of the detuning δ and Rabi splitting:

$$\delta = \omega - \frac{g^2\mu}{\pi} \int d\mathbf{r} K_0 \left(\frac{r\sqrt{\epsilon_b/R_X}}{a_X} \right) \delta(\mathbf{r}) + \epsilon_b \quad (34a)$$

$$\Omega = 2g\varphi_{1s}^{B=0}(0), \quad (34b)$$

where $\varphi_{1s}^{B=0}(0)$ is the exciton wavefunction at zero separation in absence of magnetic field and light-matter coupling. The integral in Eq. (34a) is formally divergent and it exactly cancels out the divergence on the right-hand side of Eq. (29b) when the bare photon energy ω is written in terms of the renormalized photon detuning

δ . Instead, Eq. (34b) does not diverge, as $\varphi_{1s}^{B=0}(r)$ has a well defined limit for $r \rightarrow 0$.

Introducing these definitions into Eq. (29), we can now carry out the same change of variable $\mathbf{r} \mapsto \boldsymbol{\rho} \mapsto \boldsymbol{\kappa}$ considered in Sec. III in absence of strong light-matter coupling, so that the coupled equations to solve are:

$$4\pi\bar{E} \sum_{\boldsymbol{\kappa}'} \frac{\bar{\varphi}_{\boldsymbol{\kappa}'}}{|\boldsymbol{\kappa} - \boldsymbol{\kappa}'|} - \kappa^2 \bar{\varphi}_{\boldsymbol{\kappa}} - 4\omega_c^2 \bar{\varphi}_{\boldsymbol{\kappa}} - \sum_{\boldsymbol{\kappa}'} \tilde{V}_{|\boldsymbol{\kappa} - \boldsymbol{\kappa}'|} \bar{\varphi}_{\boldsymbol{\kappa}'} = \frac{\bar{\Omega}}{4\bar{\varphi}_{1s}^{B=0}(0)} \gamma \quad (35a)$$

$$\left[\bar{E} - \bar{\delta} - \left(\frac{\bar{\Omega}}{2\sqrt{2}\varphi_{1s}^{B=0}(0)} \right)^2 \sum_{\boldsymbol{\kappa}} F(\boldsymbol{\kappa}; \bar{\epsilon}_b) + \bar{\epsilon}_b \right] \gamma = \frac{\bar{\Omega}}{2\bar{\varphi}_{1s}^{B=0}(0)} \sum_{\boldsymbol{\kappa}} \bar{\varphi}_{\boldsymbol{\kappa}}, \quad (35b)$$

where, as before we rescale quantities by the Rydberg energy and Bohr radius (20), so that $\bar{\varphi}_{1s}^{B=0}(0) = a_X \varphi_{1s}^{B=0}(0)$, $\bar{\Omega} = \Omega/R_X$, $\bar{\delta} = \delta/R_X$, and $\bar{\epsilon}_b = \epsilon_b/R_X$, and where

$$F(\boldsymbol{\kappa}; \bar{\epsilon}_b) = \frac{1}{\kappa^2} + \frac{\bar{\epsilon}_b \pi}{\kappa^3} \left[Y_0 \left(\frac{2\bar{\epsilon}_b}{\kappa} \right) - H_0 \left(\frac{2\bar{\epsilon}_b}{\kappa} \right) \right]. \quad (36)$$

As we did for the exciton case, we can numerically solve the coupled equations (35) by diagonalization once we have discretized the rescaled momentum $\boldsymbol{\kappa}$ on a grid and applied the subtraction trick described in appendix B. The normalization (28) can be implemented by the rescaling

$$\bar{\varphi}_{\boldsymbol{\kappa}} \rightarrow \bar{\varphi}_{\boldsymbol{\kappa}}/\mathcal{N} \quad \gamma \rightarrow \gamma/\mathcal{N}, \quad (37)$$

where $\mathcal{N}^2 = 8\pi \sum_{\boldsymbol{\kappa}, \boldsymbol{\kappa}'} \frac{\bar{\varphi}_{\boldsymbol{\kappa}} \bar{\varphi}_{\boldsymbol{\kappa}'}}{|\boldsymbol{\kappa} - \boldsymbol{\kappa}'|} + |\gamma|^2$. As for the exciton problem, the polariton energy E can be converted back into an eigenvalue by matrix inversion.

In Fig. 6(a) we show the polariton energy spectrum at a fixed magnetic field as a function of the exciton-photon detuning for two different values of the Rabi splitting Ω . The polariton energies display the expected anticrossing behavior, with the LP interpolating between the photon and the $1s$ exciton state, while the excited UP states interpolate between the ns and the $(n+1)s$ exciton states. The hybridization between different exciton states is evident when the Rabi splitting becomes comparable with the exciton binding energy.

Similarly, to quantify the changes in the matter component of polaritons induced by coupling to light, we examine in Fig. 6(b) the detuning dependence of the corresponding electron-hole root-mean-square separation. This is defined as

$$\frac{\langle r^2 \rangle_{\varphi}}{a_X^2} \equiv \int d\mathbf{r} \frac{r^2 |\varphi(r)|^2}{a_X^2 (1 - |\gamma|^2)} = \sum_{\boldsymbol{\kappa}} \frac{32 |\bar{\varphi}_{\boldsymbol{\kappa}}|^2}{1 - |\gamma|^2}, \quad (38)$$

where the term $1 - |\gamma|^2$ in the denominator comes from the normalization condition (28). Similarly to what observed in III-V heterostructures [17], we find that the

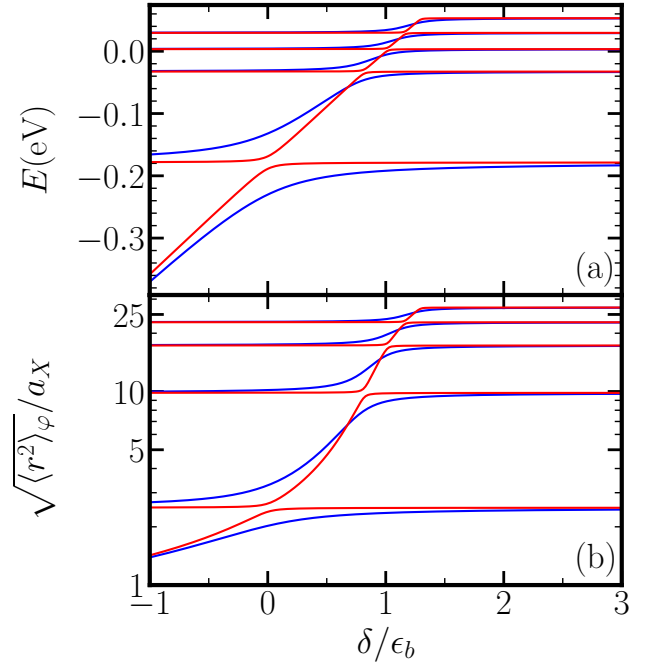


FIG. 6. (a) Polariton energies and (b) average electron-hole separation as a function of the exciton-photon detuning for the first five polariton states at fixed magnetic field $B = 30$ T and Rabi coupling $\Omega = 20$ meV (red) and $\Omega = 100$ meV (blue). From bottom to top, the lines in the two panels correspond to the same states. System parameters for hBN-encapsulated WS₂ monolayer are listed in Table I and $a_X = 0.66$ nm.

electron-hole separation in the LP is always smaller than that of the $1s$ uncoupled exciton size, with a deviation that increases with negative detunings when the LP becomes more photonic-like. At positive detuning, deviations from the $1s$ size increase for larger Ω . For excited polariton states, the electron-hole separation interpolates as a function of detuning between the ns and the $(n+1)s$ uncoupled exciton sizes, with a typical avoided crossing behavior with larger splitting when the Rabi coupling Ω increases.

We analyze the behavior of the polariton diamagnetic shift in Fig. 7. Our numerically exact results show that, as a function of detuning, the diamagnetic shifts of the different polariton branches interpolate near monotonically between the diamagnetic shifts of two adjacent excitonic states — in the case of the LP, the interpolation is between zero, as the photon mode is insensitive to the magnetic field and the diamagnetic shift of the $1s$ excitonic state. Note that, for the parameter choice of Fig. 7a, the diamagnetic shift of the LP branch is in the μeV scale and thus almost imperceptible in the meV scale of Fig. 7a. For the first excited UP state there is a very small non-monotonicity of the diamagnetic shift, which is progressively lifted with increasing values of Ω . This behavior originates from two competing effects, namely

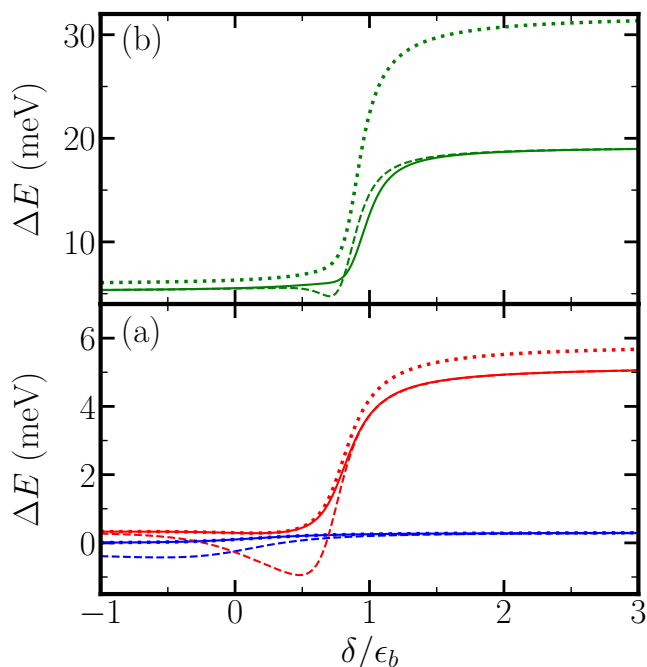


FIG. 7. Diamagnetic shift for the first 3 polariton states as a function of detuning at $B = 30$ T and Rabi coupling $\Omega = 100$ meV: LP (blue), first excited UP (red) are plotted in panel (a), while the second excited UP state is shown in panel (b). Solid lines are the numerically exact results, dashed lines are those obtained with a 4-COM (40), i.e., perturbative results in the coupling to light, and dotted lines correspond to perturbation theory in the magnetic field (39). System parameters for hBN-encapsulated WS₂ monolayer are listed in Table I.

the non-monotonic change of the photon fraction and the increase of the electron-hole distance with increasing detuning.

It is instructive to compare our numerical results with two perturbative approaches, one treating the magnetic field perturbatively and the other neglecting the light-induced modifications of the exciton wavefunction. In the first case one can use the following perturbative expression for the polariton diamagnetic shift [17]:

$$\Delta E \simeq \frac{1}{2} \mu \omega_c^2 \langle r^2 \rangle_{pol} = \frac{1}{2} \mu \omega_c^2 (1 - |\gamma|^2) \langle r^2 \rangle_{\varphi}, \quad (39)$$

where $\langle r^2 \rangle_{\varphi}$ is defined in Eq. (38). This approximation is expected to work well only when light mixes with those excitonic states well described by the small B expansion (17), i.e., for our choice of parameters, the $1s$ exciton state only. Note that it captures the qualitative behavior of the diamagnetic shift with the detuning at a fixed magnetic field, but can give quantitatively wrong results. Thus, as shown in Fig. 7a, it describes the LP state for all values of detunings and the first excited UP state for detunings $\delta < \epsilon_b$, while it fails at larger detunings as light couples additionally with the $2s$ exciton state. Naturally, for the second excited UP polariton state shown

in Fig. 7b, this perturbative approach fails in the whole range of detuning.

The second perturbative approximation employed involves neglecting the light-induced modifications of the exciton wavefunction. This approximation is expected to work well only when $\Omega \ll \epsilon_b$, while it provides qualitatively incorrect results for the diamagnetic shift and, in some cases, physically inaccurate outcomes [17] when Ω is comparable to ϵ_b . In this perturbative approach, we calculate the energies E_{ns} and oscillator strengths $\varphi_{ns}(0)/\varphi_{ns}^{B=0}(0)$ of the exciton states in absence of light-matter coupling using the methods described in Sec. III. Then, if we want to describe the first n polariton states, we include these parameters in a $n + 1$ -coupled oscillator model (COM). For example, in order to describe the first three polariton states, we can consider a 4-COM:

$$\begin{pmatrix} E_{1s} & 0 & 0 & \Omega_{1s}/2 \\ 0 & E_{2s} & 0 & \Omega_{2s}/2 \\ 0 & 0 & E_{3s} & \Omega_{3s}/2 \\ \Omega_{1s}/2 & \Omega_{2s}/2 & \Omega_{3s}/2 & \delta - \epsilon_b \end{pmatrix}, \quad (40)$$

where $\Omega_{ns} = \Omega \varphi_{ns}(0)/\varphi_{ns}^{B=0}(0)$. From the eigenvalues of this matrix one can evaluate the perturbative diamagnetic shifts shown in Fig. 7. The comparison with the exact results illustrate that the 4-COM fails to describe qualitatively the diamagnetic shift and, for the LP and first excited UP, even leads to an unphysical negative diamagnetic shift. For the first and second excited UP polariton states the diamagnetic shift grows non-monotonically due to the competition between the exciton fraction $1 - |\gamma|^2$ and the average electron-hole separation $\langle r^2 \rangle_{\varphi}$ — see Eq. (39). The non-monotonic behavior is progressively lifted for increasing values of Ω , since it increases the average electron-hole separation of the excited UP states — see Fig. 6(b). The COM is not able to recover this behavior since it does not consider the back action of light on matter and predicts instead an unphysical negative detuning. This problem cannot be solved by increasing the number of coupled oscillators [17]. Comparing our numerical results with perturbative approaches in either light-matter coupling or magnetic field effects highlights the need to go beyond these methods and employ our microscopic and exact theory.

V. EXCITON INTERACTION STRENGTH

We now turn to the interaction properties of magnetoexcitons in TMD monolayers and in III-V and II-VI QWs. To this end, we employ the Born approximation which has been demonstrated [59] to set an upper limit on the exciton-exciton interaction strength for identical ground-state excitons where no biexciton bound state exists. This allows us to extend the results of Ref. [60, 61] to TMD monolayers, where interactions are described by the Rytova-Keldysh potential, and to a finite magnetic field. Importantly, we find that for TMD monolayer excitons at zero magnetic field, the use of hydrogenic vari-

ational wavefunctions [40] gives qualitatively wrong results for the exciton-exciton interaction dependence on the screening length r_0 .

Within the Born approximation, one approximates the

$$\langle X_0^2 | X_0^2 \rangle = 2 - \frac{2}{\mathcal{A}^2} \int d\mathbf{r}_e d\mathbf{r}_h d\mathbf{r}'_e d\mathbf{r}'_h e^{-i[\frac{e}{2c}\mathbf{B} \times (\mathbf{r}_e - \mathbf{r}'_e)] \cdot (\mathbf{r}_h - \mathbf{r}'_h)} \varphi^*(|\mathbf{r}'_e - \mathbf{r}'_h|) \varphi^*(|\mathbf{r}_e - \mathbf{r}_h|) \varphi(|\mathbf{r}'_e - \mathbf{r}_h|) \varphi(|\mathbf{r}_e - \mathbf{r}'_h|). \quad (42)$$

Here, $\varphi(r)$ is the exciton wavefunction describing the electron-hole relative motion and satisfying the Schrödinger equation (16); in practice, $\varphi(r)$ is determined by solving the Schrödinger equation (22) in the rescaled reciprocal space κ , and then transform back $\kappa \mapsto \rho \mapsto r$ to real space. Note that the second term in the above normalization arises from the fact that the operator \hat{X}_0 only approximately satisfies bosonic commutation relations due to its composite nature. Note also that the normalization (42) has two terms, the first scales as $O(\mathcal{A}^0)$ in the area, while the second is $O(\mathcal{A}^{-1})$, since one can show that only 3 of the 4 real space integrals are independent.

As in previous work [47, 60–62], we perform our calculations by evaluating the energy of two excitons as twice the energy of a single exciton E plus the interaction energy between two excitons:

$$\frac{\langle X_0^2 | \hat{H}_m | X_0^2 \rangle}{\langle X_0^2 | X_0^2 \rangle} = 2E + \frac{g_{XX}}{\mathcal{A}}. \quad (43)$$

$$\frac{g_{XX}}{\mathcal{A}} = -\frac{1}{\mathcal{A}^2} \int d\mathbf{r}_e d\mathbf{r}_h d\mathbf{r}'_e d\mathbf{r}'_h e^{-i\frac{e}{2c}[\mathbf{B} \times (\mathbf{r}'_e - \mathbf{r}_e)] \cdot (\mathbf{r}'_h - \mathbf{r}_h)} [V(|\mathbf{r}_e - \mathbf{r}_h|) + V(|\mathbf{r}'_e - \mathbf{r}'_h|) - V(|\mathbf{r}_e - \mathbf{r}'_e|) - V(|\mathbf{r}_h - \mathbf{r}'_h|)] \times \varphi^*(|\mathbf{r}_e - \mathbf{r}_h|) \varphi^*(|\mathbf{r}'_e - \mathbf{r}'_h|) \varphi(|\mathbf{r}'_e - \mathbf{r}_h|) \varphi(|\mathbf{r}_e - \mathbf{r}'_h|). \quad (45)$$

Using the appropriate change of variables, it can be easily seen that the integrand of Eq. (45) depends only on three integration variables, and that this term scales as inverse area, as it should. Further, one can show that Eq. (45) is real. Equation (45) recovers known results in the limit of zero magnetic field. In particular, $g_{XX}^{B=0}$ coincides with the electron-exchange contribution to the exciton interaction obtained in Ref. [60], as the direct and exciton-exchange terms are zero for zero transferred momentum. Further, as discussed in the next section, when this expression is rewritten in momentum space, it coincides with the one derived in Ref. [61].

exact two-exciton state by that of uncorrelated excitons

$$|X_0^2\rangle = \hat{X}_0^\dagger \hat{X}_0^\dagger |0\rangle, \quad (41)$$

where the creation operator of a zero momentum exciton \hat{X}_0^\dagger is defined in Eq. (12). This state has a normalization given by

The last term comes from the interaction energy $g_{XX} N(N-1)/2\mathcal{A}$ of $N=2$ identical bosons which scales as the inverse system area \mathcal{A} . Note that we are neglecting the momentum transfer between excitons. Since the direct interaction vanishes at zero transferred momentum [63], this implies that we are only including exchange interactions. This is reasonable since the region of small momenta is the most relevant for the optical excitation, where the exchange interaction dominates [60, 61, 63]. We can extract the exciton-exciton interaction strength from Eq. (43). Because the second term of the normalization $\langle X_0^2 | X_0^2 \rangle$ (42) is of order $O(\mathcal{A}^{-1})$, as first observed in Ref. [47], we arrive at the following approximated expression of the exciton-exciton interaction strength:

$$\frac{g_{XX}}{\mathcal{A}} \simeq \frac{1}{2} \langle X_0^2 | \hat{H}_m | X_0^2 \rangle - E \langle X_0^2 | X_0^2 \rangle. \quad (44)$$

One can show that the terms of $O(1)$ on the r.h.s. of this expression cancel with each other, leaving only the correct contribution $O(\mathcal{A}^{-1})$. We obtain the following final expression for the exciton-exciton interaction strength:

In the following, we divide the discussion of results by considering first the case of zero magnetic field in Sec. VA and then finite magnetic field in Sec. VB. We will compare the results obtained for TMD monolayers with those obtained for GaAs quantum wells, for which one can employ a pure Coulomb interaction. Note that we consider exclusively the interaction properties of the lowest energy exciton state, i.e., the $1s$ state. This is because the Born approximation provides an upper bound to the interaction strength for this state [59], while being an uncontrolled approximation for excited states.

A. Zero magnetic field

In the absence of a magnetic field, it is convenient to rewrite Eq. (45) in momentum space,

$$\frac{g_{XX}^{B=0}}{\mathcal{A}} = \frac{1}{\mathcal{A}^3} \sum_{\mathbf{k}, \mathbf{k}'} V_{|\mathbf{k}-\mathbf{k}'|} |\varphi_{\mathbf{k}}|^2 |\varphi_{\mathbf{k}'}|^2 - \frac{1}{\mathcal{A}^3} \sum_{\mathbf{k}, \mathbf{k}'} V_{|\mathbf{k}-\mathbf{k}'|} \varphi_{\mathbf{k}}^* \varphi_{\mathbf{k}'}^* \varphi_{\mathbf{k}}^2 \varphi_{\mathbf{k}'}^2, \quad (46)$$

where $V_{\mathbf{k}} = \int d\mathbf{r} e^{-i\mathbf{k}\cdot\mathbf{r}} V(r)$ and $\varphi_{\mathbf{k}} = \int d\mathbf{r} e^{-i\mathbf{k}\cdot\mathbf{r}} \varphi(r)$ are the Fourier transforms from real \mathbf{r} to momentum space \mathbf{k} . As already shown in Ref. [47], this expression coincides with the expression derived in Ref. [61]. As expected, when $r_0 \rightarrow 0$, one recovers the result for a pure Coulomb potential [61]:

$$\frac{g_{XX}^{hyd}}{\mathcal{A}} = \frac{6.0566}{2\mu}. \quad (47)$$

This result is universal, in the sense that it depends only on the exciton reduced mass, but not on the exciton Rydberg energy (20).

When we instead consider the case of the Rytova-Keldysh potential, we find that the effect of the screening length r_0 is to reduce the value of $g_{XX}^{B=0}$, which monotonically decreases as a function of r_0 , see Fig. 8. Note that $g_{XX}^{B=0}/g_{XX}^{hyd}$ depends universally on the rescaled screening length r_0/a_X , remaining independent of the specific parameters chosen. For the specific case of hBN-encapsulated WS₂ considered throughout this work, we obtain an exciton interaction strength

$$\frac{g_{XX}^{B=0}|_{\text{WS}_2}}{\mathcal{A}} = \frac{5.39}{2\mu}. \quad (48)$$

This result contradicts that obtained from a variational approach based on the hydrogenic exciton state with a trial Bohr radius, which instead predicted an increase of the interaction strength with increasing r_0 [40].

The qualitatively different results reveal the sensitivity of the integrals in Eq. (46) to the exact shape of the exciton wavefunction, as shown in Fig. 3, while the exciton energy and size are largely insensitive to the precise wavefunction, see Fig. 2. Reference [40] explained their calculated increase of $g_{XX}^{B=0}$ as due to the characteristic non-local screening of the Rytova-Keldysh potential, which leads to the spreading of the electron-hole wavefunction in real space. From Fig. 3, it is evident that such a spreading does occur, although it is also clear that the exact exciton wavefunction does not exhibit a hydrogenic shape. The difference in shape is particularly pronounced near $r = 0$, where the interaction potential diverges. We note that the spreading of the wavefunction increases the absolute value of each term in the expression (46), however, as we have shown, their difference actually decreases with increasing r_0 . We thus conclude

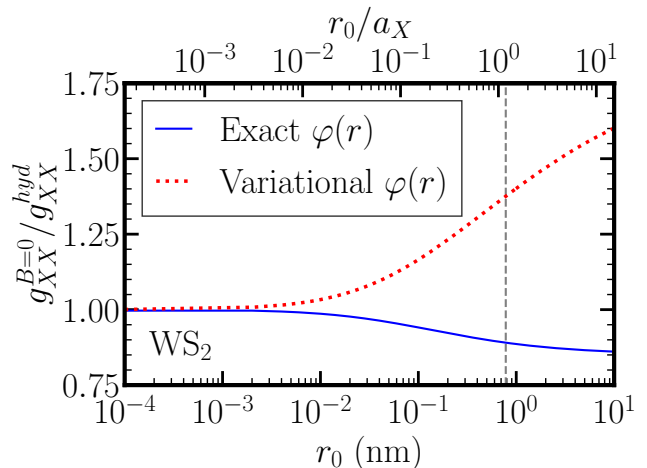


FIG. 8. Screening length dependence of the exciton-exciton interaction strength for hBN-encapsulated WS₂ at zero magnetic field. The interaction strength is calculated within the Born approximation and is normalized by g_{XX}^{hyd} (47), i.e., the corresponding exciton-exciton interaction strength for pure Coulomb interaction. Our numerically exact evaluation of Eq. (46) (blue solid line) is compared with that obtained with a variational calculation (red dotted line) as in Ref. [40]. The vertical dashed line indicates the value of r_0 describing the hBN-encapsulated WS₂ monolayer, see Table I and $a_X = 0.66$ nm. The scale of the upper x -axis is the rescaled screening length.

that the non-hydrogenic shape plays a role just as important as the average electron-hole separation when computing the interaction strength, thus highlighting the necessity of using the exact wavefunctions in the calculation of the exciton-exciton interaction strength.

B. Finite magnetic field

For finite values of the magnetic field, we evaluate numerically the exciton-exciton interaction strength (45) employing a multidimensional Monte Carlo method [55].³ Because of the large values of the $1s$ binding energy in TMD monolayers, the diamagnetic shift of the $1s$ state is small and varies in the μeV range for magnetic field values as high as 60 T — see Sec. III 2. Because of this, we also expect that g_{XX} has a weak dependence on the magnetic field. For example, for WS₂ parameters, at the largest magnetic field considered in this work, $B = 60$ T, we obtain only a 6.5% reduction of the inter-

³ We have checked that, in the zero magnetic field limit, the results obtained with Monte Carlo integration and those obtained by using Eq. (46) coincide within the statistical error of the Monte Carlo integration.

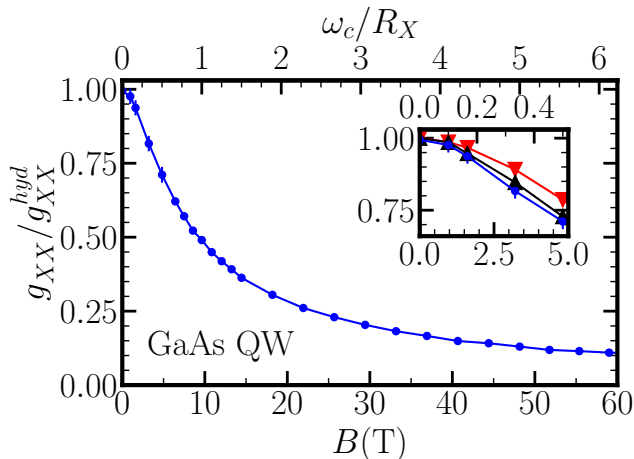


FIG. 9. Magnetic field dependence of the exciton-exciton interaction strength (45) for a GaAs QW. In the inset, the small field behavior of our results (blue circles) is compared with the interaction evaluated using the hydrogenic wavefunction $\varphi_{1s}^{hyd}(r)$ (A2) (red down-triangles), as well as a small-field perturbative expansion to first order of the wavefunction (18) (black upper-triangles). The scale of the upper x -axis is the rescaled cyclotron frequency. The errorbars of the numerical results (due to statistical error of the Monte Carlo method — see text) are only visible for very small values of the magnetic field. Parameters for the GaAs QW are listed in Table I.

action strength compared to the $B = 0$ case (48):

$$\frac{g_{XX}^{B=60\text{ T}}}{\mathcal{A}} \Big|_{\text{WS}_2} = \frac{5.04 \pm 0.02}{2\mu}. \quad (49)$$

The error is the statistical error estimate from Monte Carlo integration. The small decrease of g_{XX} with increasing magnetic field is partially due to the reduction of the exciton size (see Fig. 5b). As discussed next, the other factor that comes into play resides in the exponential term $e^{-i\frac{e}{2c}[\mathbf{B} \times (\mathbf{r}'_e - \mathbf{r}_e)] \cdot (\mathbf{r}'_h - \mathbf{r}_h)}$ in Eq. (51), which originates from the Lamb transformation (12) of the exciton state.

Unlike TMDs, GaAs QWs display significant changes in g_{XX} for experimentally accessible values of the magnetic field. Using the typical parameters listed in Table I, we plot in Fig. 9 the magnetic field dependence of the exciton-exciton interaction strength. Here, we observe that already at $\omega_c = 0.5R_X$ ($B = 4.82$ T) the exciton-exciton interaction strength is reduced by 28.5% compared with the value at $B = 0$ (g_{XX}^{hyd}), while at $\omega_c = 6R_X$ ($B = 57.8$ T) the reduction is 89.0%. Note that, for pure Coulomb interactions, the dependence of g_{XX}/g_{XX}^{hyd} on the rescaled cyclotron frequency ω_c/R_X is universal and independent of the chosen parameters, such as the exciton reduced mass and Rydberg energy.

In order to determine which factor primarily contributes to the reduced exciton-exciton interaction strength with increasing magnetic field, we plot in the inset of Fig. 9 the low-field behavior of the interaction

strength. Here, we compare our numerically exact evaluation of Eq. (45) with two approximations: In the first, the interaction is evaluated using the hydrogenic wavefunction $\varphi_{1s}^{hyd}(r)$ (A2) so that the sole effect of the magnetic field is included in the exponential term $e^{-i\frac{e}{2c}[\mathbf{B} \times (\mathbf{r}'_e - \mathbf{r}_e)] \cdot (\mathbf{r}'_h - \mathbf{r}_h)}$. In the second, the interaction is evaluated by using instead the low-field perturbative expansion of the wavefunction to first order (18). Clearly, the three results agree in the $B \rightarrow 0$ limit. Notably, the first approximation already describes a decrease of the interaction strength with the magnetic field, indicating that the mere presence of the exponential in the integrand leads to a reduction of the interaction strength. Including perturbatively the effects of the magnetic field in the exciton wavefunction improves the behavior of the interaction strength with respect to the previous result, approaching the exact result when $B \lesssim 2$ T.

VI. POLARITON INTERACTION STRENGTH

We finally examine the interaction properties of magnetopolaritons in microcavities containing either TMD monolayers or III-V heterostructures. Interactions between polaritons are inherited from their matter component. Indeed, the hybrid nature of cavity polaritons allows for the possibility of low-mass and strongly interacting quasiparticles. Besides, since magnetic fields can be employed to enhance the coupling of exciton states to light [10, 11], we are especially interested in understanding how these interactions are affected by a static transverse magnetic field. As for excitons, we employ a Born approximation, which sets an upper bound on the polariton-polariton interaction strength [59] for identical excitons (we do not consider the case of polaritons of different spin, for which one needs to go beyond the Born approximation [64]). Furthermore, exact four-body calculations show that the Born approximation becomes more precise as the Rabi coupling increases [65].

It was already shown in Ref. [47] for pure Coulomb interaction that approaches neglecting the light-induced modifications of the electron-hole wavefunction [60–62, 66, 67] overestimate polariton-polariton interactions in the very strong light-matter coupling regime. We extend the results of Ref. [47] to the case of TMD monolayers and to a finite magnetic field. Our approach employs the exact polariton wavefunctions obtained in Sec. IV, thus treating the coupling to light and the magnetic field on the same footing.

The derivation of the polariton-polaritons interaction strength follows the same steps employed in Sec. V for the exciton-exciton interaction strength. In particular, to obtain the Born approximation we consider the uncorrelated two-polariton state:

$$|P_0^2\rangle = \hat{P}_0^\dagger \hat{P}_0^\dagger |0\rangle. \quad (50)$$

where \hat{P}_0^\dagger is the creation operator of a zero momentum polariton defined in Eq. (27). The normalization of this

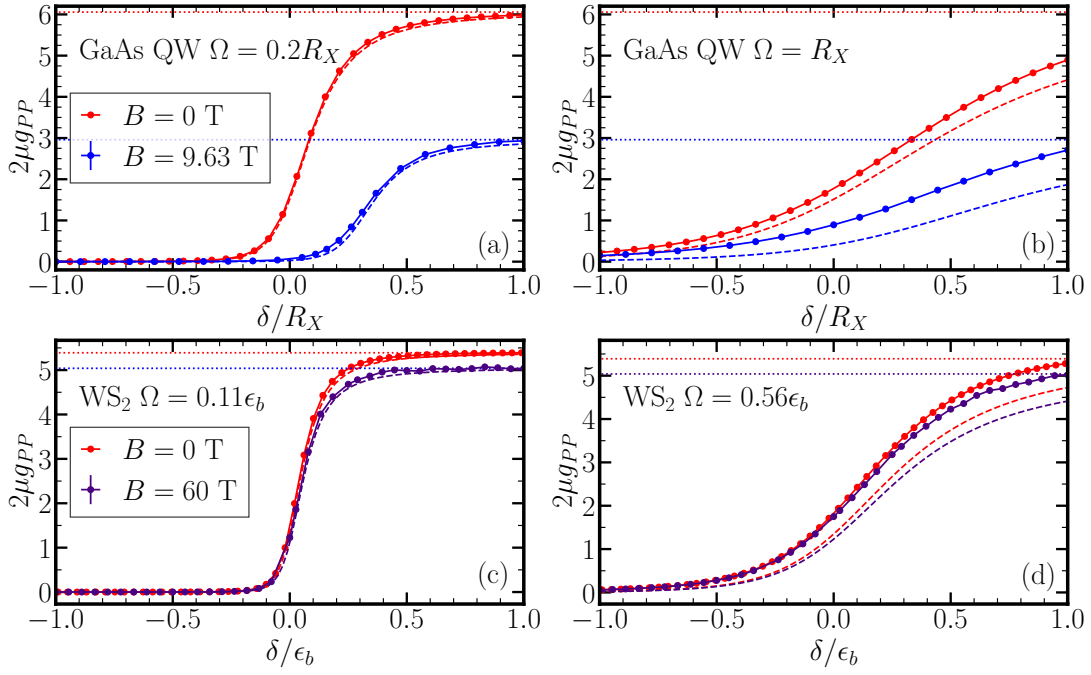


FIG. 10. Detuning dependence of the polariton-polariton interaction strength for a GaAs QW (a,b) and an hBN-encapsulated WS₂ monolayer (c,d). Parameters are listed in Table I. For GaAs QW, g_{PP} is calculated at $B = 0$ T and $B = 10.72$ T (corresponding to $\omega_c = R_X$), and for two different values of the Rabi splitting: (a) $\Omega = 2.7$ meV = $0.2R_X$; (b) $\Omega = 13.5$ meV = R_X . For WS₂, g_{PP} is calculated at $B = 0$ T and $B = 60$ T and for two different values of the Rabi splitting: (c) $\Omega = 20$ meV = $0.11\epsilon_b$; (d) $\Omega = 100$ meV = $0.56\epsilon_b$. Our numerically exact Born approximation (circles) are compared with the perturbative expression (52) (dashed lines). The horizontal dotted lines correspond to the exciton-exciton interaction strength g_{XX} evaluated using Eqs. (45) and (46). The errorbars due to statistical error of the Monte Carlo method of the numerical results (see text) are not visible on the scale of the figure.

state is identical to Eq. (42), where, however, $\varphi(r)$ is now the wavefunction describing the electron and hole relative motion within the polariton state. $\varphi(r)$ and the photon amplitude γ are obtained by solving the cou-

pled equations (35) in κ -space and transforming back to r -space. By following the same steps that led to the exciton-exciton interaction strength (45) in Sec. V, for polaritons we obtain:

$$\begin{aligned} \frac{g_{PP}}{\mathcal{A}} = & -\frac{1}{\mathcal{A}^2} \int d\mathbf{r}_e d\mathbf{r}_h d\mathbf{r}'_e d\mathbf{r}'_h e^{-i\frac{\epsilon}{2c}[\mathbf{B} \times (\mathbf{r}'_e - \mathbf{r}_e)] \cdot (\mathbf{r}'_h - \mathbf{r}_h)} [V(|\mathbf{r}_e - \mathbf{r}_h|) + V(|\mathbf{r}'_e - \mathbf{r}'_h|) - V(|\mathbf{r}_e - \mathbf{r}'_e|) - V(|\mathbf{r}_h - \mathbf{r}'_h|)] \\ & \times \varphi^*(|\mathbf{r}_e - \mathbf{r}_h|) \varphi^*(|\mathbf{r}'_e - \mathbf{r}'_h|) \varphi(|\mathbf{r}'_e - \mathbf{r}_h|) \varphi(|\mathbf{r}_e - \mathbf{r}'_h|) - \frac{2g\gamma^*}{\mathcal{A}} \int d\mathbf{r}_1 d\mathbf{r}_2 e^{\frac{-i\epsilon}{2c}[\mathbf{B} \times \mathbf{r}_1] \cdot \mathbf{r}_2} \varphi(r_1) \varphi(r_2) \varphi^*(|\mathbf{r}_1 - \mathbf{r}_2|). \end{aligned} \quad (51)$$

The first term of this expression coincides with the exciton-exciton interaction strength (45). The second term instead derives exclusively from the light-matter coupling and is zero in the absence of light-matter coupling, i.e., $g_{XX} = g_{PP}|_{\Omega=0}$. In the zero magnetic field limit, the expression (51) is more conveniently written in momentum space k in which case it recovers the result derived in Ref. [47].

We consider the combined effects of very strong light-matter coupling and a strong magnetic field on the interaction properties between magnetopolaritons for both

multiple GaAs quantum wells [12] and multiple WS₂ monolayers [28] embedded into a microcavity. Figure 10 shows our results as a function of detuning. Here we compare the results at zero and finite magnetic field, as well as those for two different Rabi splittings corresponding to the strong and very-strong coupling regimes. For GaAs QW, parameters are those characterizing the experiments of Ref. [12], while for WS₂ monolayers, we adopt parameters compatible with those of the experiment of Ref. [28]. In both cases, we compare the numerical results obtained by evaluating Eq. (51) with the

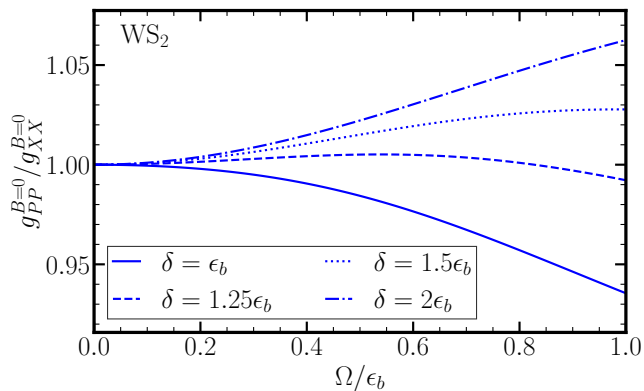


FIG. 11. Rabi splitting dependence of the polariton-polariton interaction strength at zero magnetic field for hBN-encapsulated WS₂ monolayer for several values of the detuning δ . See system parameters in Table I.

perturbative expression valid in the regime of perturbative light-matter coupling, where the excitonic component within the polariton is assumed to be unmodified by the coupling to light:

$$g_{PP}^{(0)} = \beta^4 g_{XX}. \quad (52)$$

Here, $\beta^2 = 1 - \gamma_{LP}^2$ is the exciton fraction of polaritons valid within the 2-COM (31), where the expression of the Hopfield coefficient γ_{LP} is given in Eq. (33). As discussed in Sec. IV, the perturbative expression (52) is expected to be accurate in the limit $\Omega \ll \epsilon_b$ [61].

In both figures, we observe that the polariton-polariton interaction strength interpolates as a function of detuning between zero and the exciton-exciton interaction strength. However, the behavior deviates from a purely Hopfield factor interpolation as described by Eq. (52) when Ω is of the order of the 1s exciton binding energy. Further, as discussed later, the interpolation is not always monotonic and the polariton-polariton interaction can exceed the exciton-exciton interaction. The approximated expression (52) underestimates the value of the polariton-polariton interaction strength, with deviations from the exact results that are larger at more positive detunings. In the very strong coupling regime, when Ω is of the same order of magnitude as ϵ_b , the discrepancies between exact g_{PP} (51) and perturbative $g_{PP}^{(0)}$ (52) increases with increasing magnetic field. This is particularly visible in the case of a GaAs QW in Fig. 10b. This result is due to the increase of the exciton oscillator strength with increasing magnetic field. Consequently, higher order terms in Ω/ϵ_b beyond the leading order approximation $g_{PP}^{(0)}$ are required as the magnetic field grows. Note, however, that it was already shown in Ref. [47], that perturbative corrections due to exciton oscillator saturation [61] or photon assisted exchange processes [62] greatly overestimate the exact result at $B = 0$.

The interpolation of the polariton-polariton interaction strength as a function of detuning between zero and

the exciton-exciton interaction strength can be slightly non-monotonic and, at positive detunings, g_{PP} can reach values larger than g_{XX} . This is illustrated in Fig. 11, where we plot the dependence on the Rabi splitting of the polariton-polariton interaction strength at zero magnetic field and at large positive values of detuning for the specific case of hBN-encapsulated WS₂. We find that, at sufficiently large detuning, the polariton-polariton interaction strength first grows with Ω to larger values than the polariton-polariton interaction strength, and then eventually decreases. This implies that g_{PP} can exhibit a non-monotonic behavior as a function of detuning and fixed Rabi, approaching at large detunings g_{XX} asymptotically from above rather than from below. This result mirrors those of Refs. [64] and [65] which found a similar enhancement of the polariton interactions, with the effect being even larger when one goes beyond the Born approximation.

VII. CONCLUSIONS

In this work, we have presented a microscopic approach for TMD monolayers that allowed us to exactly describe excitons and polaritons in the presence of a perpendicular static magnetic field. Magneto-optical measurements have already been widely used in TMD monolayers to quantitatively analyze exciton properties and parameters [30–39]. Our approach provides numerically exact solutions for the ground and excited states, accommodating arbitrarily large magnetic fields, leading to an extremely good agreement with the diamagnetic shifts measured in Ref. [39]. For polaritons, we have extended our results into the very strong coupling regime, where light-induced modifications of the exciton wavefunction become critical. Here, we have shown that the diamagnetic shift of the lowest-lying polariton states at high magnetic fields carry clear signatures of the very strong coupling regime. Although no current experiments have explored TMD polaritons in this regime, we have investigated experimentally accessible parameters [28], anticipating that this will inspire future studies.

We have employed the Born approximation to evaluate the interaction properties of both excitons and polaritons in a strong magnetic field, comparing TMD structures with traditional GaAs quantum wells. In both semiconductor types, we have found that applying a magnetic field leads to a decrease of the interaction strength. For TMD excitons, we have shown that employing hydrogenic variational wavefunctions [40] results in overestimating the interaction strength, producing qualitatively inaccurate results and emphasizing the necessity of exact solutions. It would be valuable for future research to generalize our formalism to describe the interaction properties of excited states. Rydberg polariton states are gaining significant attention due to their substantial spatial extent, which is anticipated to result in significant interactions [27, 68], thus enabling blocking phenomena [69].

ACKNOWLEDGMENTS

We are grateful to Scott Crooker and Mateusz Goryca for letting us use the data from Ref. [39]. We would like to thank Jack Engdahl, Oleg Sushkov, and Dmitry Efimkin for fruitful discussions and for sharing details about their recent unpublished work, Ref. [70]. DDFP acknowledges financial support from the Ministerio de Educación, Formación Profesional y Deportes through the “Beca de Colaboración” fellowship. DDFP and FMM acknowledge financial support from the Spanish Ministry of Science, Innovation and Universities through the “Maria de Maetzu” Programme for Units of Excellence in R&D (CEX2023-001316-M) and from the Comunidad de Madrid and the Spanish State through the Recovery, Transformation and Resilience Plan [“MATERIALES DISRUP-TIVOS BIDIMENSIONALES (2D)” (MAD2D-CM)-UAM7]. FMM acknowledges financial support from the Ministerio de Ciencia e Innovación (MICINN), project No. AEI/10.13039/501100011033 PID2020-113415RB-C22 (2DEnLight) and from the Proyecto Sinérgico CAM 2020 Y2020/TCS-6545 (NanoQuCo-CM). MMP is supported through Australian Research Council Future Fellowship FT200100619. JL and MMP also acknowledge support from the Australian Research Council Centre of Excellence in Future Low-Energy Electronics and Technologies, ‘FLEET’ (CE170100039). EL is supported by a Women-in-FLEET research fellowship.

Appendix A: Two-dimensional hydrogenic solutions and variational approach for $B = 0$

In the limit where the screening length r_0 vanishes, the Rytova-Keldysh potential (6) recovers the pure Coulomb interaction. In real and momentum space this reads

$$V^C(r) = -\frac{e^2}{\varepsilon r} \quad V_k^C = -\frac{2\pi e^2}{\varepsilon k}. \quad (\text{A1})$$

In the absence of a magnetic field, the exciton states recover the 2D hydrogenic solutions [71, 72]. For s -wave solutions, the exciton energies are

$$E_{ns}^{hyd} = -\frac{R_X}{(2n-1)^2}, \quad (\text{A2})$$

and the eigenfunctions:

$$\varphi_{ns}^{hyd}(r) = \frac{1}{a_X} \sqrt{\frac{2/\pi}{(2n-1)^3}} \exp\left(\frac{-r/a_X}{2n-1}\right) L_{n-1}\left[\frac{2r/a_X}{2n-1}\right], \quad (\text{A3})$$

where the Rydberg energy R_X and exciton Bohr radius a_X have been defined in Eq. (20), and where $L_{n-1}(x)$ are the Laguerre polynomials. The mean square electron-hole separation can also be calculated analytically:

$$\langle r^2 \rangle_{ns}^{hyd} = \frac{a_X^2}{2} (2n-1)^2 (3 + 5n(n-1)). \quad (\text{A4})$$

The 2D exciton problem with a Rytova-Keldysh potential (6) does not allow for an analytical solution. However, an alternative to solving the Schrödinger equation numerically is to consider a variational approach with trial hydrogenic functions (A3), with the Bohr radius determined variationally for each ns state by minimizing the energy [23, 35, 40]:

$$a_X \mapsto \lambda_{X,ns}. \quad (\text{A5})$$

The variational Bohr radii evaluated for the hBN-encapsulated WS_2 experiments of Ref. [39] (see Table I) — and employed in Fig. 2 to compare the variational and numerically exact exciton energies and radii — are summarized in Table II.

ns	$\lambda_{X,ns}$ (nm)
1s	1.53
2s	0.88
3s	0.78
4s	0.74
5s	0.72

TABLE II. Variational exciton Bohr radius for the first five s -states. Parameters are those summarized in Table I, for which $a_X = 0.66$ nm. Note that, for growing values of n , states become more hydrogenic and $\lambda_{X,ns} \rightarrow a_X$.

Appendix B: Subtraction scheme for the Rytova-Keldysh potential

In this appendix we describe the subtraction scheme adopted to numerically solve the Schrödinger equation (22) that deals with the pole of the Rytova-Keldysh potential in rescaled momentum space, $\tilde{V}_{|\kappa-\kappa'|}$, at $\kappa = \kappa'$. Note that this method is adapted from the one developed in Ref. [17] for pure Coulomb interaction $|\kappa-\kappa'|^{-1}$. The potential \tilde{V}_κ admits the following analytical expression:

$$\tilde{V}_\kappa = -\frac{1}{9\bar{r}_0^4\kappa^{5/2}} \left\{ 128\sqrt{2}\Gamma\left(\frac{7}{4}\right)^2 \bar{r}_0^2\kappa \, {}_1F_2\left(1; \frac{5}{4}, \frac{5}{4}; -\frac{1}{\bar{r}_0^4\kappa^2}\right) + 8\sqrt{2}\Gamma\left(\frac{1}{4}\right)^2 {}_1F_2\left(1; \frac{7}{4}, \frac{7}{4}; -\frac{1}{\bar{r}_0^4\kappa^2}\right) - 9\pi^2\bar{r}_0^3\kappa^{3/2} \left[Y_0\left(\frac{2}{\bar{r}_0^2\kappa}\right) + H_0\left(\frac{2}{\bar{r}_0^2\kappa}\right) \right] \right\}, \quad (\text{B1})$$

where $\bar{r}_0 = r_0/a_X$ and where ${}_pF_q(a_1, \dots, a_p; b_1, \dots, b_q)$ is the generalized hypergeometric function, $H_0(x)$ is the zeroth-order Struve Function and $Y_0(x)$ the zeroth-order Bessel function of the second kind.

In the eigenvalue problem (22), the angular integration can be carried out for s -wave solutions, which allows us to obtain an equation that only depends on the variable κ :

$$\begin{aligned} \bar{E} \int \frac{d\kappa'\kappa'}{2\pi} \tilde{V}_1(\kappa, \kappa') \bar{\varphi}_{\kappa'} \\ = \kappa^2 \bar{\varphi}_\kappa + 4\bar{\omega}_c^2 \bar{\varphi}_\kappa + \int \frac{d\kappa'\kappa'}{2\pi} \tilde{V}_2(\kappa, \kappa') \bar{\varphi}_{\kappa'}, \end{aligned} \quad (\text{B2})$$

where

$$\tilde{V}_1(\kappa, \kappa') = \int_0^{2\pi} \frac{d\theta'}{2\pi} \frac{4\pi}{|\kappa - \kappa'|} = \frac{8}{\kappa + \kappa'} \text{K} \left[\frac{4\kappa\kappa'}{(\kappa + \kappa')^2} \right] \quad (\text{B3a})$$

$$\tilde{V}_2(\kappa, \kappa') = \int_0^{2\pi} \frac{d\theta'}{2\pi} \tilde{V}_{|\kappa - \kappa'|}, \quad (\text{B3b})$$

and where $\text{K}(x)$ is the complete elliptic integral of the first kind. While $\tilde{V}_1(\kappa, \kappa')$ can be evaluated analytically [17], $\tilde{V}_2(\kappa, \kappa')$ has to be evaluated numerically. Note that the potential $\tilde{V}_1(\kappa, \kappa')$ diverges when $\kappa' = \kappa$. However, $\tilde{V}_2(\kappa, \kappa')$ is convergent when $\kappa' = \kappa$ and diverges only when $\kappa' = \kappa = 0$. Both issues can be solved by adding and subtracting the following (diagonal) terms to Eq. (B2):⁴

$$\int_0^\infty \frac{d\kappa'\kappa'}{2\pi} \frac{2\kappa^2}{\kappa^2 + \kappa'^2} \left[\bar{E} \tilde{V}_1(\kappa, \kappa') + \tilde{V}_2(\kappa, \kappa') \right] \bar{\varphi}_\kappa. \quad (\text{B4})$$

The prefactor $\frac{2\kappa^2}{\kappa^2 + \kappa'^2}$ is 1 at $\kappa = \kappa'$, while it decays as $\sim (\kappa')^{-2}$ when $\kappa' \rightarrow \infty$, thus speeding up convergence. At the same time, the terms (B4) that we subtract exactly cancels the divergences of Eq. (B2), while the terms we add are convergent. In particular, the following integral can be evaluated analytically:

$$\int_0^\infty \frac{d\kappa'\kappa'}{2\pi} g_1(\kappa, \kappa') = \frac{\kappa}{\sqrt{2}} \frac{\Gamma\left(\frac{1}{4}\right)^2}{\Gamma\left(\frac{1}{2}\right)}, \quad (\text{B5})$$

⁴ Strictly speaking, the subtraction scheme is redundant for the potential $\tilde{V}_2(\kappa, \kappa')$ as we only need to remove the divergence at $\kappa' = \kappa = 0$. Nevertheless, we find that including it aids with convergence.

while the other integral can be conveniently rewritten as follows

$$\int_0^\infty \frac{d\kappa'\kappa'}{2\pi} g_2(\kappa, \kappa') = -\frac{2\pi}{\bar{r}_0} \kappa^2 I(\kappa), \quad (\text{B6})$$

where

$$\begin{aligned} I(\kappa) = \int_0^\infty d\rho J_0(\kappa\rho) K_0(\kappa\rho) \\ \times \left[H_0\left(\frac{\sqrt{8\rho}}{\bar{r}_0}\right) - Y_0\left(\frac{\sqrt{8\rho}}{\bar{r}_0}\right) \right]. \end{aligned}$$

This integral is evaluated numerically.

Appendix C: Exciton diamagnetic shift for the MoSe₂, MoS₂, and MoTe₂ monolayer data of Ref. [39]

In the main text we showed the excellent agreement between our theoretical results and the experimental data of Ref. [39] on the diamagnetic shift of hBN-encapsulated WS₂ monolayer. In this appendix we include the comparison for other TMD monolayers in Fig. 12, namely MoTe₂ (a), MoSe₂ (b), and MoS₂ (c). The parameters employed to describe these materials have been taken from Ref. [39] and are indicated in each figure caption, with small variations on the energy bandgap (< 0.1%) for a better comparison. As for the case of WS₂, we observe an excellent agreement.

Appendix D: Finite orbital angular momentum exciton states

We can generalize the results presented in the main text for s -wave excitons and obtain the Rydberg series with finite orbital angular momentum. To this end, we begin with Eq. (14) and set $\mathbf{K} = 0$, while keeping l_z finite. The exciton Schrödinger equation now reads

$$E\varphi(\mathbf{r}) = \left[-\frac{1}{2\mu} \nabla_{\mathbf{r}}^2 + \frac{\mu\omega_c^2}{2} r^2 + V(r) \right] \varphi(\mathbf{r}), \quad (\text{D1})$$

where $\mathbf{r} = (r, \theta)$. We remark that we have neglected the term (15a) since $m_e \simeq m_h$ in TMD monolayers, but it is straightforward to include since it simply yields a

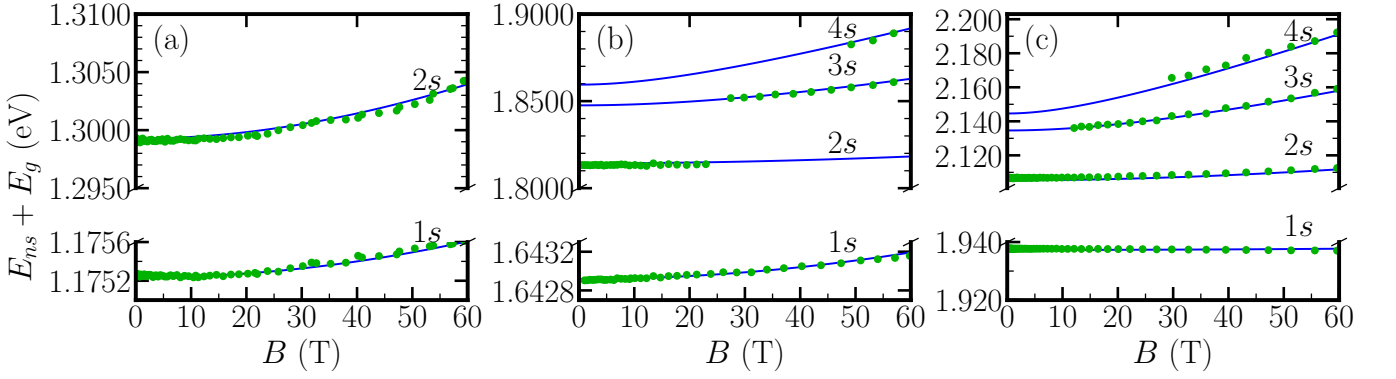


FIG. 12. Comparison between theoretical (solid lines) and experimental data of Ref. [39] (symbols) of the exciton diamagnetic shift of different TMD monolayers. (a) hBN-encapsulated MoTe₂ monolayer with parameters $r_0 = 1.45$ nm, $\mu = 0.36m_0$, $\varepsilon = 4.4$, and $E_g = 1.35212$ eV. (b) hBN-encapsulated MoSe₂ monolayer with parameters $r_0 = 0.89$ nm, $\mu = 0.350m_0$, $\varepsilon = 4.4$, and $E_g = 1.87488$ eV. (c) hBN-encapsulated MoS₂ monolayer with parameters $r_0 = 0.76$ nm, $\mu = 0.28m_0$, $\varepsilon = 4.5$, and $E_g = 2.157$ eV. Note that the energy scale relevant for the 1s state is different from that of the excited states to better show variations.

Zeeman shift of $[(\omega_{c,e} - \omega_{c,h})/2]l_z$ for the two states with a given $|l_z| \neq 0$.⁵

By introducing the rescaled real space variables $\boldsymbol{\rho} = (\rho = r^2/(8a_X^2), \phi = 2\theta)$, we obtain the following dimensionless equation in rescaled real space:

$$\frac{2\bar{E}}{\rho}\bar{\varphi}(\boldsymbol{\rho}) = \left[-\nabla_{\boldsymbol{\rho}}^2 + 4\bar{\omega}_c^2 + \tilde{V}(\boldsymbol{\rho})\right]\bar{\varphi}(\boldsymbol{\rho}). \quad (\text{D2})$$

Fourier transforming this expression into rescaled reciprocal space yields

$$\bar{E} \sum_{\boldsymbol{\kappa}'} \frac{4\pi\bar{\varphi}_{\boldsymbol{\kappa}'}}{|\boldsymbol{\kappa} - \boldsymbol{\kappa}'|} = (\kappa^2 + 4\bar{\omega}_c^2)\bar{\varphi}_{\boldsymbol{\kappa}} + \sum_{\boldsymbol{\kappa}'} \tilde{V}_{|\boldsymbol{\kappa} - \boldsymbol{\kappa}'|}\bar{\varphi}_{\boldsymbol{\kappa}'}. \quad (\text{D3})$$

Above, $\sum_{\boldsymbol{\kappa}} \equiv \int d\boldsymbol{\kappa}/(2\pi)^2 = \int_0^\infty d\kappa \kappa/(2\pi) \int_0^{2\pi} d\phi/(2\pi)$ and $\boldsymbol{\kappa} = (\kappa, \phi)$, while $\tilde{V}_{\boldsymbol{\kappa}}$ is defined in Eq. (B1). If we now expand the exciton wavefunction $\bar{\varphi}_{\boldsymbol{\kappa}}$ over the orbital angular momentum basis $e^{i\ell\phi}$,

$$\bar{\varphi}_{\boldsymbol{\kappa}} \equiv \bar{\varphi}_{\kappa\phi} = \sum_{\ell \in \mathbb{Z}} e^{i\ell\phi} \tilde{\varphi}_{\kappa\ell}, \quad (\text{D4})$$

then Eq. (D3) becomes

$$\bar{E} \int_0^\infty \frac{d\kappa' \kappa'}{2\pi} V_1(\kappa, \kappa', \ell) \tilde{\varphi}_{\kappa'\ell} = (\kappa^2 + 4\bar{\omega}_c^2) \tilde{\varphi}_{\kappa\ell} + \int_0^\infty \frac{d\kappa' \kappa'}{2\pi} V_2(\kappa, \kappa', \ell) \tilde{\varphi}_{\kappa'\ell}. \quad (\text{D5})$$

This result involves the matrix kernels,

$$V_1(\kappa, \kappa', \ell) = 4\pi \int_0^{2\pi} \frac{d\phi'}{2\pi} \frac{\cos(\ell\phi')}{|\boldsymbol{\kappa} - \boldsymbol{\kappa}'|}, \quad (\text{D6a})$$

$$V_2(\kappa, \kappa', \ell) = \int_0^{2\pi} \frac{d\phi'}{2\pi} \cos(\ell\phi') \tilde{V}_{|\boldsymbol{\kappa} - \boldsymbol{\kappa}'|}, \quad (\text{D6b})$$

where ϕ' is the angle of $\boldsymbol{\kappa}'$ measured relative to $\boldsymbol{\kappa}$. Note that Eq. (D5) is diagonal in ℓ since $[\hat{H}'_m, \hat{L}_z] = 0$, and thus, the equation conserves orbital angular momentum.

Due to the redefinition of the angle $\theta \mapsto \phi = 2\theta$ in the $\mathbf{r} \mapsto \boldsymbol{\rho}$ change of variables, only *even* partial wave states can be accessed by solving the $\boldsymbol{\kappa}$ -space equation (D5): setting $\ell = 0, \pm 1, \pm 2, \dots$ gives $l_z = 0, \pm 2, \pm 4, \dots$, i.e., the s, d, g, \dots Rydberg exciton series.⁶ Odd partial wave states would instead need to be obtained by solving the Schrödinger equation in either real \mathbf{r} space or momentum \mathbf{k} space, both of which are less convenient approaches owing to the presence of derivatives. The subtraction scheme discussed in Ref. [17] and Appendix B can be employed to deal with the Coulomb-like pole in the $V_1(\kappa, \kappa', \ell)$ matrix kernel (D6a). Numerically integrating over the angle in $V_2(\kappa, \kappa', \ell)$ (D6b) can be very time consuming due to the complicated form of the Rytova–Keldysh potential in $\boldsymbol{\kappa}$ space (B1). This process can be sped up significantly first by tabulating the value of $\tilde{V}_{\boldsymbol{\kappa}}$ versus κ on a logarithmic grid and interpolating to populate the three-dimensional matrix kernel, and then by performing Gauss–Legendre quadrature in the angular direction.

Figure 13(a) displays the energies of the Rydberg series of d -wave excitons as functions of the magnetic field,

⁵ The effective electron and hole masses for different monolayer TMDs have been calculated from first principles and presented in Table 5 of Ref. [73]. By using the values for WS₂, the Zeeman shift for d -wave excitons ($l_z = \pm 2$) at a magnetic field of $B = 60$ T, for example, is around $\sim \pm 1.44$ meV.

⁶ Notice that since the even partial waves are periodic on 2π , the upper limits of the angular integrals in Eqs. (D3) and (D5)–(D6) remain as 2π , consistent with the s -wave ($l_z = \ell = 0$) case.

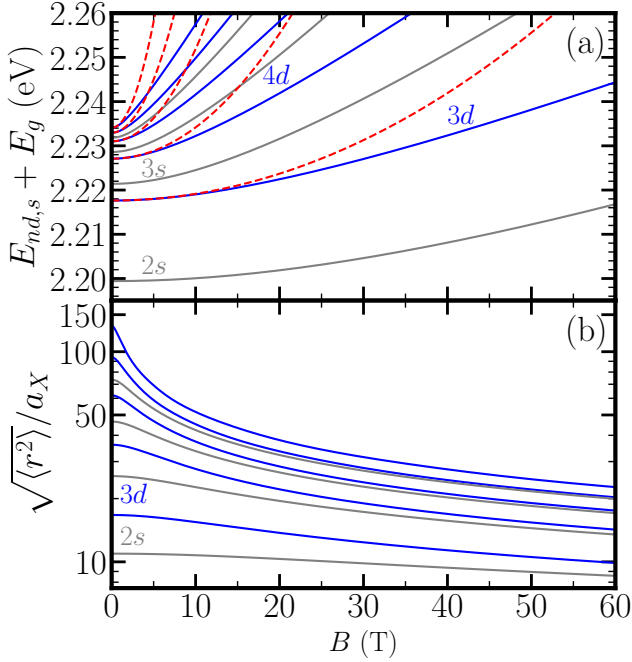


FIG. 13. Magnetic field dependence of the first five nd ($n = 3, \dots, 7$) Rydberg exciton energies (a) and root-mean-square radii (b) obtained from the numerically exact solution of Eq. (D5) with $\ell = 1$ (solid blue lines). In panel (a) the dashed red lines are the perturbation theory results in the weak magnetic field limit (D7). In both panels the ns exciton series ($n = 2, \dots, 5$) is also shown as a reference (gray lines). All parameters are for hBN-encapsulated WS₂ as reported in Ref. [39] (see Table I and $a_X = 0.66$ nm), with an energy gap of $E_g = 2.23725$ eV.

overlaid on the s -wave exciton energies for comparison. In the limit where both $B \rightarrow 0$ and $r_0 \rightarrow 0$, we recover the ‘accidental degeneracy’ of the two-dimensional hydrogen atom [72]. In this case, for each energy level labelled by the principal quantum number $n = 1, 2, \dots$, there is a $(2n - 1)$ -fold degeneracy:

$n = 1$	$1s$	(1-fold)
2	$2s, 2p$	(3-fold)
3	$3s, 3p, 3d$	(5-fold)
4	$4s, 4p, 4d, 4f$	(7-fold)

Consistent with Figs. 2–5 on magnetoexcitons in the main text, the dimensionless screening length in Fig. 13(a) has a finite value of $r_0/a_X \simeq 1.18$, which breaks this degeneracy at zero magnetic field, leading to small observable differences between the $3s$ and $3d$ energies, and between the $4s$ and $4d$ energies, etc. In the opposite limit of strong magnetic fields, the electron-hole interaction potential can effectively be neglected and we instead recover the degeneracies of the Landau levels, i.e., of the two-dimensional harmonic oscillator. Now, for a given harmonic oscillator index $N = 0, 1, 2, \dots$, there is an $(N + 1)$ -fold degeneracy:

$N = 0$	$1s$	(1-fold)
1	$2p$	(2-fold)
2	$2s, 3d$	(3-fold)
3	$3p, 4f$	(4-fold)
4	$3s, 4d, 5g$	(5-fold)

Here, the labelling refers to the weak-field states, i.e., how they are adiabatically connected at large B .⁷ We can see that the parity of N matches whether the angular momentum is even (s, d, g, \dots) or odd (p, f, \dots). Our transformation $\mathbf{r} \mapsto \boldsymbol{\rho}$ captures only the even angular momenta, and thus only even N , since $N = 2(n-1) - |l_z|$. In the high-field limit, the eigenenergies depend linearly on the exciton cyclotron frequency ω_c . By plotting and overlaying E_{ns}/ω_c and E_{nd}/ω_c versus ω_c/R_X , we have checked that the $\{2s, 3d\}$ energies approach the same value for increasing ω_c/R_X ($\gtrsim 0.1$), as do the $\{3s, 4d\}$, $\{4s, 5d\}$, and $\{5s, 6d\}$ energies.

Also shown in Fig 13(a) are the results from first-order non-degenerate perturbation theory in the weak-field regime:

$$E_{nd} \simeq E_{nd}^{B=0} + \frac{\mu\omega_c^2}{2} \langle r^2 \rangle_{nd}. \quad (\text{D7})$$

Here, $\langle r^2 \rangle_{nd}$ is the mean-square radius of the exciton at zero magnetic field, which is determined by applying the partial wave expansion (D4) both to the following result,

$$\frac{\langle r^2 \rangle}{a_X^2} = \frac{1}{a_X^2} \int d\mathbf{r} r^2 |\varphi(\mathbf{r})|^2 = 32 \sum_{\boldsymbol{\kappa}} |\bar{\varphi}_{\boldsymbol{\kappa}}|^2, \quad (\text{D8})$$

and to the normalization condition on the wavefunction: $\bar{\varphi}_{\boldsymbol{\kappa}} \rightarrow \bar{\varphi}_{\boldsymbol{\kappa}}/\mathcal{N}$ where $\mathcal{N}^2 = 8\pi \sum_{\boldsymbol{\kappa}, \boldsymbol{\kappa}'} \bar{\varphi}_{\boldsymbol{\kappa}} \bar{\varphi}_{\boldsymbol{\kappa}'}^* / |\boldsymbol{\kappa} - \boldsymbol{\kappa}'|$. Similar to the s -wave case, for more highly excited states, the perturbative energies are accurate for a narrower range of fields. In other words, as the magnetic field increases, higher excited states approach the strong-field regime more quickly than less excited states. Figure 13(b) displays the root-mean-square electron-hole separation for the d -wave Rydberg exciton series. Again consistent with the s -wave case, it can be seen that the exciton size decreases with increasing magnetic field (and increasing binding energy), with the effect more pronounced for higher excited states. At strong fields, the s - and d -wave states which tend towards the same radius match the degeneracies in the energy spectrum discussed above.

Exciton states with finite orbital angular momentum are optically dark with regard to conventional one-photon detection [74]; however they may be observed through a consequence of the Stark effect. By applying a weak static in-plane electric field, one can couple to states that

⁷ We clarify that these high-field degeneracies differ from those in Ref. [6]. There, the authors consider the different problem of a conduction electron interacting with a donor (i.e., an infinitely heavy hole), and therefore the $\mathcal{O}(l_z)$ term (15a) is present, which leads to the altered degeneracies shown in their Table III.

differ by a single quantum of angular momentum [52]. If the electric field is treated perturbatively, then the leading order element describes the coupling of the s exciton to the p exciton, which causes the latter to shift slightly in energy and become brighter. The next or-

der element then describes the application of a stronger electric field, whereby the d exciton also couples in and becomes brighter. Alternatively, excitonic dark states can be probed in TMD monolayers by using two-photon excitation spectroscopy [51].

-
- [1] N. Miura, *Physics of Semiconductors in High Magnetic Fields* (Oxford University Press, 2007).
- [2] S. Tarucha, H. Okamoto, Y. Iwasa, and N. Miura, *Exciton binding energy in GaAs quantum wells deduced from magneto-optical absorption measurement*, *Solid State Communications* **52**, 815 (1984).
- [3] M. Bugajski, W. Kuzsko, and K. Regiński, *Diamagnetic shift of exciton energy levels in GaAs-Ga_{1-x}Al_xAs quantum wells*, *Solid State Communications* **60**, 669 (1986).
- [4] J. Warnock, A. Petrou, R. N. Bicknell, N. C. Giles-Taylor, D. K. Blanks, and J. F. Schetzina, *Photoluminescence of Cd_{1-x}Mn_xTe-CdTe multiple-quantum-well structures and superlattices in a magnetic field*, *Phys. Rev. B* **32**, 8116 (1985).
- [5] E. L. Ivchenko, A. V. Kavokin, V. P. Kochereshko, G. R. Posina, I. N. Uraltsev, D. R. Yakovlev, R. N. Bicknell-Tassius, A. Waag, and G. Landwehr, *Exciton oscillator strength in magnetic-field-induced spin superlattices CdTe/(Cd,Mn)Te*, *Phys. Rev. B* **46**, 7713 (1992).
- [6] A. H. MacDonald and D. S. Ritchie, *Hydrogenic energy levels in two dimensions at arbitrary magnetic fields*, *Phys. Rev. B* **33**, 8336 (1986).
- [7] W. Edelstein, H. N. Spector, and R. Marasas, *Two-dimensional excitons in magnetic fields*, *Phys. Rev. B* **39**, 7697 (1989).
- [8] C. Stafford, S. Schmitt-Rink, and W. Schaefer, *Nonlinear optical response of two-dimensional magnetoexcitons*, *Phys. Rev. B* **41**, 10000 (1990).
- [9] J. Tignon, P. Voisin, C. Delalande, M. Voos, R. Houdré, U. Oesterle, and R. P. Stanley, *From Fermi's Golden Rule to the Vacuum Rabi Splitting: Magnetopolaritons in a Semiconductor Optical Microcavity*, *Phys. Rev. Lett.* **74**, 3967 (1995).
- [10] B. Pietka, D. Zygmont, M. Król, M. R. Molas, A. A. L. Nicolet, F. Morier-Genoud, J. Szczytko, J. Lusakowski, P. Zikeba, I. Tralle, P. Stkepnicki, M. Matuszewski, M. Potemski, and B. Deveaud, *Magnetic field tuning of exciton-polaritons in a semiconductor microcavity*, *Phys. Rev. B* **91**, 075309 (2015).
- [11] B. Pietka, M. R. Molas, N. Bobrovska, M. Król, R. Mirek, K. Lekenta, P. Stkepnicki, F. Morier-Genoud, J. Szczytko, B. Deveaud, M. Matuszewski, and M. Potemski, *2s exciton-polariton revealed in an external magnetic field*, *Phys. Rev. B* **96**, 081402 (2017).
- [12] S. Brodbeck, S. De Liberato, M. Amthor, M. Klaas, M. Kamp, L. Worschech, C. Schneider, and S. Höfling, *Experimental Verification of the Very Strong Coupling Regime in a GaAs Quantum Well Microcavity*, *Phys. Rev. Lett.* **119**, 027401 (2017).
- [13] D. M. Whittaker, T. A. Fisher, A. M. Afshar, M. S. Skolnick, P. Kinsler, J. S. Roberts, G. Hill, and M. A. Pate, *Vacuum rabi splitting in semiconductor microcavities with applied electric and magnetic fields*, *Il Nuovo Cimento D* **17**, 1781 (1995).
- [14] T. A. Fisher, A. M. Afshar, M. S. Skolnick, D. M. Whittaker, and J. S. Roberts, *Vacuum Rabi coupling enhancement and Zeeman splitting in semiconductor quantum microcavity structures in a high magnetic field*, *Phys. Rev. B* **53**, R10469 (1996).
- [15] J. D. Berger, O. Lyngnes, H. M. Gibbs, G. Khitrova, T. R. Nelson, E. K. Lindmark, A. V. Kavokin, M. A. Kaliteevski, and V. V. Zapasskii, *Magnetic-field enhancement of the exciton-polariton splitting in a semiconductor quantum-well microcavity: The strong coupling threshold*, *Phys. Rev. B* **54**, 1975 (1996).
- [16] M.-J. Yang, N. Y. Kim, Y. Yamamoto, and N. Na, *Verification of very strong coupling in a semiconductor optical microcavity*, *New Journal of Physics* **17**, 023064 (2015).
- [17] E. Laird, F. M. Marchetti, D. K. Efimkin, M. M. Parish, and J. Levinsen, *Rydberg exciton-polaritons in a magnetic field*, *Phys. Rev. B* **106**, 125407 (2022).
- [18] G. Wang, A. Chernikov, M. M. Glazov, T. F. Heinz, X. Marie, T. Amand, and B. Urbaszek, *Colloquium: Excitons in atomically thin transition metal dichalcogenides*, *Rev. Mod. Phys.* **90**, 021001 (2018).
- [19] J. R. Schaibley, H. Yu, G. Clark, P. Rivera, J. S. Ross, K. L. Seyler, W. Yao, and X. Xu, *Valleytronics in 2D materials*, *Nature Reviews Materials* **1**, 16055 (2016).
- [20] K. F. Mak and J. Shan, *Photonics and optoelectronics of 2D semiconductor transition metal dichalcogenides*, *Nature Photonics* **10**, 216 (2016).
- [21] Y. Liu, Y. Gao, S. Zhang, J. He, J. Yu, and Z. Liu, *Valleytronics in transition metal dichalcogenides materials*, *Nano Research* **12**, 2695 (2019).
- [22] A. Ramasubramaniam, *Large excitonic effects in monolayers of molybdenum and tungsten dichalcogenides*, *Phys. Rev. B* **86**, 115409 (2012).
- [23] T. C. Berkelbach, M. S. Hybertsen, and D. R. Reichman, *Theory of neutral and charged excitons in monolayer transition metal dichalcogenides*, *Phys. Rev. B* **88**, 045318 (2013).
- [24] A. Chernikov, T. C. Berkelbach, H. M. Hill, A. Rigosi, Y. Li, B. Aslan, D. R. Reichman, M. S. Hybertsen, and T. F. Heinz, *Exciton Binding Energy and Nonhydrogenic Rydberg Series in Monolayer WS₂*, *Phys. Rev. Lett.* **113**, 076802 (2014).
- [25] X. Liu, T. Galfsky, Z. Sun, F. Xia, E.-c. Lin, Y.-H. Lee, S. Kéna-Cohen, and V. M. Menon, *Strong light-matter coupling in two-dimensional atomic crystals*, *Nature Photonics* **9**, 30 (2015).
- [26] S. Dufferwiel, S. Schwarz, F. Withers, A. A. P. Trichet, F. Li, M. Sich, O. Del Pozo-Zamudio, C. Clark, A. Nalitov, D. D. Solnyshkov, G. Malpuech, K. S. Novoselov, J. M. Smith, M. S. Skolnick, D. N. Krizhanovskii, and A. I. Tartakovskii, *Exciton-polaritons in van der Waals heterostructures embedded in tunable microcavities*, *Nature Communications* **6**, 8579 (2015).
- [27] J. Gu, V. Walther, L. Waldecker, D. Rhodes, A. Raja,

- J. C. Hone, T. F. Heinz, S. Kéna-Cohen, T. Pohl, and V. M. Menon, *Enhanced nonlinear interaction of polaritons via excitonic Rydberg states in monolayer WSe₂*, *Nature Communications* **12**, 2269 (2021).
- [28] J. Zhao, A. Fieramosca, K. Dini, R. Bao, W. Du, R. Su, Y. Luo, W. Zhao, D. Sanvitto, T. C. H. Liew, and Q. Xiong, *Exciton polariton interactions in Van der Waals superlattices at room temperature*, *Nature Communications* **14**, 1512 (2023).
- [29] A. Arora, *Magneto-optics of layered two-dimensional semiconductors and heterostructures: Progress and prospects*, *Journal of Applied Physics* **129**, 120902 (2021).
- [30] A. A. Mitioglu, P. Plochocka, Á. Granados del Aguila, P. C. M. Christianen, G. Deligeorgis, S. Anghel, L. Kulyuk, and D. K. Maude, *Optical Investigation of Monolayer and Bulk Tungsten Diselenide (WSe₂) in High Magnetic Fields*, *Nano Letters* **15**, 4387 (2015).
- [31] G. Plechinger, P. Nagler, A. Arora, A. Granados del Águila, M. V. Ballottin, T. Frank, P. Steinleitner, M. Gmitra, J. Fabian, P. C. M. Christianen, R. Bratschkitsch, C. Schüller, and T. Korn, *Excitonic Valley Effects in Monolayer WS₂ under High Magnetic Fields*, *Nano Letters* **16**, 7899 (2016), pMID: 27960453.
- [32] A. V. Stier, N. P. Wilson, G. Clark, X. Xu, and S. A. Crooker, *Probing the Influence of Dielectric Environment on Excitons in Monolayer WSe₂: Insight from High Magnetic Fields*, *Nano Letters* **16**, 7054 (2016).
- [33] A. V. Stier, K. M. McCreary, B. T. Jonker, J. Kono, and S. A. Crooker, *Exciton diamagnetic shifts and valley Zeeman effects in monolayer WS₂ and MoS₂ to 65 Tesla*, *Nature Communications* **7**, 10643 (2016).
- [34] A. V. Stier, N. P. Wilson, K. A. Velizhanin, J. Kono, X. Xu, and S. A. Crooker, *Magneto-optics of Exciton Rydberg States in a Monolayer Semiconductor*, *Phys. Rev. Lett.* **120**, 057405 (2018).
- [35] J. Zipfel, J. Holler, A. A. Mitioglu, M. V. Ballottin, P. Nagler, A. V. Stier, T. Taniguchi, K. Watanabe, S. A. Crooker, P. C. M. Christianen, T. Korn, and A. Chernikov, *Spatial extent of the excited exciton states in WS₂ monolayers from diamagnetic shifts*, *Phys. Rev. B* **98**, 075438 (2018).
- [36] J. Have, N. M. R. Peres, and T. G. Pedersen, *Excitonic magneto-optics in monolayer transition metal dichalcogenides: From nanoribbons to two-dimensional response*, *Phys. Rev. B* **100**, 045411 (2019).
- [37] E. Liu, J. van Baren, T. Taniguchi, K. Watanabe, Y.-C. Chang, and C. H. Lui, *Magnetophotoluminescence of exciton Rydberg states in monolayer WSe₂*, *Phys. Rev. B* **99**, 205420 (2019).
- [38] A. Delhomme, G. Butseraen, B. Zheng, L. Marty, V. Bouchiat, M. R. Molas, A. Pan, K. Watanabe, T. Taniguchi, A. Ouerghi, J. Renard, and C. Faugeras, *Magneto-spectroscopy of exciton Rydberg states in a CVD grown WSe₂ monolayer*, *Applied Physics Letters* **114**, 232104 (2019).
- [39] M. Goryca, J. Li, A. V. Stier, T. Taniguchi, K. Watanabe, E. Courtade, S. Shree, C. Robert, B. Urbaszek, X. Marie, and S. A. Crooker, *Revealing exciton masses and dielectric properties of monolayer semiconductors with high magnetic fields*, *Nature Communications* **10**, 4172 (2019).
- [40] V. Shahnazaryan, I. Iorsh, I. A. Shelykh, and O. Kyriienko, *Exciton-exciton interaction in transition-metal dichalcogenide monolayers*, *Phys. Rev. B* **96**, 115409 (2017).
- [41] N. Rytova, *The screened potential of a point charge in a thin film*, *Moscow University Physics Bulletin* **3**, 18 (1967).
- [42] L. V. Keldysh, *Coulomb interaction in thin semiconductor and semimetal films*, *Soviet Journal of Experimental and Theoretical Physics Letters* **29**, 658 (1979).
- [43] J. Wierzbowski, J. Klein, F. Sigger, C. Straubinger, M. Kremser, T. Taniguchi, K. Watanabe, U. Wurstbauer, A. W. Holleitner, M. Kaniber, K. Müller, and J. J. Finley, *Direct exciton emission from atomically thin transition metal dichalcogenide heterostructures near the lifetime limit*, *Scientific Reports* **7**, 12383 (2017).
- [44] F. Cadiz, E. Courtade, C. Robert, G. Wang, Y. Shen, H. Cai, T. Taniguchi, K. Watanabe, H. Carrere, D. Lagarde, M. Manca, T. Amand, P. Renucci, S. Tongay, X. Marie, and B. Urbaszek, *Excitonic Linewidth Approaching the Homogeneous Limit in MoS₂-Based van der Waals Heterostructures*, *Phys. Rev. X* **7**, 021026 (2017).
- [45] P. Cudazzo, I. V. Tokatly, and A. Rubio, *Dielectric screening in two-dimensional insulators: Implications for excitonic and impurity states in graphene*, *Phys. Rev. B* **84**, 085406 (2011).
- [46] D. Van Tuan, M. Yang, and H. Dery, *Coulomb interaction in monolayer transition-metal dichalcogenides*, *Phys. Rev. B* **98**, 125308 (2018).
- [47] J. Levinsen, G. Li, and M. M. Parish, *Microscopic description of exciton-polaritons in microcavities*, *Phys. Rev. Res.* **1**, 033120 (2019).
- [48] A. Delteil, T. Fink, A. Schade, S. Höfling, C. Schneider, and A. İmamoğlu, *Towards polariton blockade of confined exciton-polaritons*, *Nature Materials* **18**, 219 (2019).
- [49] W. E. Lamb, *Fine Structure of the Hydrogen Atom. III*, *Phys. Rev.* **85**, 259 (1952).
- [50] L. P. Gor'kov and I. E. Dzyaloshinskii, *Contribution to the Theory of the Mott Exciton in a Strong Magnetic Field*, *Soviet Journal of Experimental and Theoretical Physics* **26**, 449 (1968).
- [51] Z. Ye, T. Cao, K. O'Brien, H. Zhu, X. Yin, Y. Wang, S. G. Louie, and X. Zhang, *Probing excitonic dark states in single-layer tungsten disulphide*, *Nature* **513**, 214 (2014).
- [52] B. Zhu, K. Xiao, S. Yang, K. Watanabe, T. Taniguchi, and X. Cui, *In-Plane Electric-Field-Induced Orbital Hybridization of Excitonic States in Monolayer WSe₂*, *Phys. Rev. Lett.* **131**, 036901 (2023).
- [53] I. H. Duru and H. Kleinert, *Quantum Mechanics of H-Atom from Path Integrals*, *Fortschritte der Physik* **30**, 401 (1982).
- [54] C. Klingshirm, *Semiconductor Optics*, Graduate Texts in Physics (Springer Berlin Heidelberg, 2012).
- [55] W. H. Press, S. A. Teukolsky, W. T. Vetterling, and B. P. Flannery, *Numerical Recipes 3rd Edition: The Art of Scientific Computing*, 3rd ed. (Cambridge University Press, USA, 2007).
- [56] L. Landau and E. Lifshitz, *Quantum Mechanics: Non-Relativistic Theory*, Course of theoretical physics (Elsevier Science, 1991).
- [57] J. Bloch, T. Freixanet, J. Y. Marzin, V. Thierry-Mieg, and R. Planel, *Giant Rabi splitting in a microcavity containing distributed quantum wells*, *Applied Physics Letters* **73**, 1694 (1998).

- [58] M. Saba, C. Ciuti, J. Bloch, V. Thierry-Mieg, R. André, L. S. Dang, S. Kundermann, A. Mura, G. Bongiovanni, J. L. Staehli, and B. Deveaud, *High-temperature ultrafast polariton parametric amplification in semiconductor microcavities*, *Nature* **414**, 731 (2001).
- [59] G. Li, O. Bleu, J. Levinsen, and M. M. Parish, *Theory of polariton-electron interactions in semiconductor microcavities*, *Phys. Rev. B* **103**, 195307 (2021).
- [60] C. Ciuti, V. Savona, C. Piermarocchi, A. Quattropani, and P. Schwendimann, *Role of the exchange of carriers in elastic exciton-exciton scattering in quantum wells*, *Phys. Rev. B* **58**, 7926 (1998).
- [61] F. Tassone and Y. Yamamoto, *Exciton-exciton scattering dynamics in a semiconductor microcavity and stimulated scattering into polaritons*, *Phys. Rev. B* **59**, 10830 (1999).
- [62] M. Combescot, M. A. Dupertuis, and O. Betbeder-Matibet, *Polariton-polariton scattering: Exact results through a novel approach*, *Europhysics Letters* **79**, 17001 (2007).
- [63] D. Erkensten, S. Brem, and E. Malic, *Exciton-exciton interaction in transition metal dichalcogenide monolayers and van der Waals heterostructures*, *Phys. Rev. B* **103**, 045426 (2021).
- [64] O. Bleu, G. Li, J. Levinsen, and M. M. Parish, *Polariton interactions in microcavities with atomically thin semiconductor layers*, *Phys. Rev. Research* **2**, 043185 (2020).
- [65] G. Li, M. M. Parish, and J. Levinsen, *Microscopic calculation of polariton scattering in semiconductor microcavities*, *Phys. Rev. B* **104**, 245404 (2021).
- [66] G. Rochat, C. Ciuti, V. Savona, C. Piermarocchi, A. Quattropani, and P. Schwendimann, *Excitonic Bloch equations for a two-dimensional system of interacting excitons*, *Phys. Rev. B* **61**, 13856 (2000).
- [67] M. M. Glazov, H. Ouerdane, L. Piloizzi, G. Malpuech, A. V. Kavokin, and A. D'Andrea, *Polariton-polariton scattering in microcavities: A microscopic theory*, *Phys. Rev. B* **80**, 155306 (2009).
- [68] M. Makhonin, A. Delphan, K. W. Song, P. Walker, T. Isoniemi, P. Claronino, K. Orfanakis, S. K. Rajendran, H. Ohadi, J. Heckötter, M. Assmann, M. Bayer, A. Tartakovskii, M. Skolnick, O. Kyriienko, and D. Krizhanovskii, *Nonlinear Rydberg exciton-polaritons in Cu₂O microcavities*, *Light: Science & Applications* **13**, 47 (2024).
- [69] J. Heckötter, V. Walther, S. Scheel, M. Bayer, T. Pohl, and M. Afmann, *Asymmetric Rydberg blockade of giant excitons in Cuprous Oxide*, *Nature Communications* **12**, 3556 (2021).
- [70] J. N. Engdahl, H. D. Scammell, D. K. Efimkin, and O. P. Sushkov, *Excitons in Atomically Thin TMD in Electric and Magnetic Fields* (2024), arXiv:2409.18373.
- [71] X. L. Yang, S. H. Guo, F. T. Chan, K. W. Wong, and W. Y. Ching, *Analytic solution of a two-dimensional hydrogen atom. I. Nonrelativistic theory*, *Phys. Rev. A* **43**, 1186 (1991).
- [72] D. G. W. Parfitt and M. E. Portnoi, *The two-dimensional hydrogen atom revisited*, *Journal of Mathematical Physics* **43**, 4681 (2002).
- [73] F. A. Rasmussen and K. S. Thygesen, *Computational 2D Materials Database: Electronic Structure of Transition-Metal Dichalcogenides and Oxides*, *The Journal of Physical Chemistry C* **119**, 13169 (2015).
- [74] M. Rohlfing and S. G. Louie, *Electron-hole excitations and optical spectra from first principles*, *Phys. Rev. B* **62**, 4927 (2000).